REPORT DOCUMENTATION PAGE

Form Approved OMB NO. 0704-0188

1. REPORT DATE (DD-MM-YYYY)	2. REPORT TYPE	3. DATES COVERED (From - To)
30-01-2022	Final Report	1-Jul-2016 - 31-Oct-2020

4. TITLE AND SUBTITLE
Final Report: The Optomechanical Response of Nanostructured Materials

5a. CONTRACT NUMBER
W911NF-16-1-0359

5b. GRANT NUMBER

5c. PROGRAM ELEMENT NUMBER
611102

6. AUTHORS

5d. PROJECT NUMBER

5e. TASK NUMBER

5f. WORK UNIT NUMBER

7. PERFORMING ORGANIZATION NAMES AND ADDRESSES
Purdue University
Sponsored Program Services
155 S Grant Street
West Lafayette, IN 47907 -2114

8. PERFORMING ORGANIZATION REPORT NUMBER

9. SPONSORING/MONITORING AGENCY NAME(S) AND ADDRESS (ES)
U.S. Army Research Office
P.O. Box 12211
Research Triangle Park, NC 27709-2211

10. SPONSOR/MONITOR'S ACRONYM(S)
ARO

11. SPONSOR/MONITOR'S REPORT NUMBER(S)
69104-PH.2

12. DISTRIBUTION AVAILIBILITY STATEMENT
Approved for public release; distribution is unlimited.

13. SUPPLEMENTARY NOTES
The views, opinions and/or findings contained in this report are those of the author(s) and should not contrued as an official Department of the Army position, policy or decision, unless so designated by other documentation.

14. ABSTRACT

15. SUBJECT TERMS

16. SECURITY CLASSIFICATION OF:			17. LIMITATION OF ABSTRACT	15. NUMBER OF PAGES	19a. NAME OF RESPONSIBLE PERSON
a. REPORT	b. ABSTRACT	c. THIS PAGE			Kevin Webb
UU	UU	UU	UU		19b. TELEPHONE NUMBER 765-494-3373

RPPR Final Report
as of 09-Feb-2022

Agency Code: 21XD

Proposal Number: 69104PH **Agreement Number: W911NF-16-1-0359**
INVESTIGATOR(S):

Name: Ph.D. Kevin Webb
Email: kevin.j.webb.1@purdue.edu
Phone Number: 7654943373
Principal: Y

Organization: **Purdue University**
Address: Sponsored Program Services, West Lafayette, IN 479072114
Country: USA
DUNS Number: 072051394 EIN: 356002041
Report Date: 31-Jan-2021 Date Received: 30-Jan-2022
Final Report for Period Beginning 01-Jul-2016 and Ending 31-Oct-2020
Title: The Optomechanical Response of Nanostructured Materials
Begin Performance Period: 01-Jul-2016 **End Performance Period:** 31-Oct-2020
Report Term: 0-Other
Submitted By: Ph.D. Kevin Webb Email: kevin.j.webb.1@purdue.edu
Phone: (765) 494-3373
Distribution Statement: 1-Approved for public release; distribution is unlimited.

STEM Degrees: **STEM Participants:**

Major Goals: This project involved the investigation of the relationship between nanostructured material and the force due to incident light and resulted in new fundamental physical understanding, facilitating a variety of application frontiers.

Accomplishments: • The relationship between the Einstein-Laub electromagnetic force and the Lorentz force on free charge has been established.
• The pressure on asymmetric 1D cavities is presented as a means to understand the basis of the pressure on structured surfaces.
• The optical force on aperiodic nano-structured material relates enhanced pushing and pulling to resonant field character.
• An experimental demonstration shows that the force on nanostructured material can exceed that on a perfect mirror.
• The regulation of top and bottom plasmon surface wave resonances is shown to produce pushing and pulling, respectively.
• An experiment to measure membrane deflection due to a force from a laser beam has been built.
• Designs for nanostructured membranes that could allow demonstration of pulling of a structure using a simple laser beam for the first time have been completed and fabrication completed.
• Initial results for all-dielectric structures that permit a pulling force are presented.
• The Einstein and Laub expression for electromagnetic force density is shown to be in agreement with the traditionally accepted Maxwell expression in the case of a plane wave normally incident on a semi-infinite planar mirror.

Training Opportunities: Graduate students Adam Behnke and Tom Pollei worked on this project most recently, and this research will constitute their Ph.D. theses. Dr. Li-Fan Yang completed his Ph.D. in 2020 and his thesis was focused on experimental and simulation-based aspects of optomechanics in nanostructured media (Optical Force Regulation with Nanostructured Materials). Dr. Yu-Chun Hsueh completed his Ph.D. in 2018 (Field Control and Optical Force Enhancement in Aperiodic Nanostructures).

Two undergraduate students were involved in this research. Jackson Gihl, a Purdue undergraduate student in the School of Electrical and Computer Engineering (ECE), worked with the Webb group under an National Science Foundation REU award. In addition, Scott Kenning, a Purdue ECE undergraduate student, has been working on modeling of membrane mechanics with laser illumination. This is relevant to understanding membrane motion in experiments and the extraction of optical force information.

RPPR Final Report
as of 09-Feb-2022

Results Dissemination: The following papers associated with this award have been published, recently presented, and submitted, or are in preparation.

1. A. H. Velzen and K. J. Webb, “Electromagnetic force on structured metallic surfaces,” Phys. Rev. B 92, 115416 (2015).
2. K. J. Webb, “Relationship between the Einstein-Laub electromagnetic force and the Lorentz force on free charge,” Phys. Rev. B 94, 064203 (2016).
3. Y.-C. Hsueh, L.-F. Yang, and K. J. Webb, “Enhanced optical pressure with asymmetric cavities,” Phys. Rev. B 99, 045437 (2019).
4. Y.-C. Hsueh, L.-F. Yang, and K. J. Webb, “Optical pressure control with aperiodic nanostructured material,” J. Opt. Soc. Am. B 36, 1408-1419 (2019).
5. L.-F. Yang, A. Datta, Y.-C. Hsueh, X. Xu, and K. J. Webb, “Demonstration of enhanced optical pressure on a structured surface,’ ’Phys. Rev. Lett. 122, 083901 (2019).
6. K. J. Webb (Invited), L.-F. Yang, A. Datta, Y.-C. Hsueh, and X. Xu, “Enhanced optical force with nanostructured material,” The 50th Winter Colloquium on the Physics of Quantum Electronics, Snowbird, UT, Jan. 5-10, 2020.
7. L.-F. Yang and K. J. Webb, “Pushing and pulling optomechanics with plasmonic surface waves,” OSA/IEEE/APS CLEO (Conference on Lasers and Electrooptics) Meeting, San Jose, CA, May 11-15, 2020 (moved to a virtual on-line meeting): Digest paper for Presentation FM4Q.3.
8. L.-F. Yang and K. J. Webb, “Pushing and pulling optical pressure control with plasmonic surface waves,” Phys. Rev. B 103, 245124 (2021).
9. T. J. Pollei, A.W. Behnke, and K. J. Webb, “Einstein-Laub force on a mirror,” In preparation and 2022 Optica/APS/IEEE CLEO conference submission.

Honors and Awards: Nothing to Report

Protocol Activity Status:

Technology Transfer: Nothing to Report

PARTICIPANTS:

Participant Type: PD/PI
Participant: Kevin Webb
Person Months Worked: 6.00 **Funding Support:**
Project Contribution:
National Academy Member: N

Participant Type: Graduate Student (research assistant)
Participant: Li-Fan Yang
Person Months Worked: 12.00 **Funding Support:**
Project Contribution:
National Academy Member: N

Participant Type: Graduate Student (research assistant)
Participant: Yu-Chun Hsueh
Person Months Worked: 12.00 **Funding Support:**
Project Contribution:
National Academy Member: N

Participant Type: Graduate Student (research assistant)
Participant: Adam Behnke

RPPR Final Report
as of 09-Feb-2022

Person Months Worked: 6.00 **Funding Support:**
Project Contribution:
National Academy Member: N

Participant Type: Graduate Student (research assistant)
Participant: Thomas Pollei
Person Months Worked: 6.00 **Funding Support:**
Project Contribution:
National Academy Member: N

Partners

,

I certify that the information in the report is complete and accurate:
Signature: Kevin John Webb
Signature Date: 1/30/22 5:30PM

Final Report
ARO Award W911NF-16-1-0359
The Optomechanical Response of Nanostructured Materials

Kevin Webb Group
Purdue University
West Lafayette, Indiana 47907, USA
webb@purdue.edu

Program Manager: Dr. James Joseph
Army Research Office

January 27, 2022

Abstract

This project involved the investigation of the relationship between nanostructured material and the force due to incident light and resulted in new fundamental physical understanding, facilitating a variety of application frontiers. Our report contains an introduction to the project in Sections 1 and 2, background on the optical force density in material, leading to pressure, in Section 3, and summaries of research results along the following lines.

- The relationship between the Einstein-Laub electromagnetic force and the Lorentz force on free charge has been established — Section 4.
- The pressure on asymmetric 1D cavities is presented as a means to understand the basis of the pressure on structured surfaces — Section 5.
- The optical force on aperiodic nano-structured material relates enhanced pushing and pulling to resonant field character — Section 6.
- An experimental demonstration shows that the force on nanostructured material can exceed that on a perfect mirror — Section 7.
- The regulation of top and bottom plasmon surface wave resonances is shown to produce pushing and pulling, respectively — Section 8.
- An experiment to measure membrane deflection due to a force from a laser beam has been built — Section 9.
- Designs for nanostructured membranes that could allow demonstration of pulling of a structure using a simple laser beam for the first time have been completed and fabrication completed — Section 10.
- Initial results for all-dielectric structures that permit a pulling force are presented — Section 11.
- The Einstein and Laub expression for electromagnetic force density is shown to be in agreement with the traditionally accepted Maxwell expression in the case of a plane wave normally incident on a semi-infinite planar mirror — Section 12.
- The broader impacts of the work on science and education are summarized — Section 13.
- The publications resulting from this research are listed — Section 14.

Contents

1 Motivation

Light from the sun supports life on earth, light is used in most communication systems, and light is used with increasing frequency in health care. In all of these domains, it is the energy aspect of light that is employed. Associated with the classical field energy is a photon momentum. More than one century ago the mechanical nature of light was measured, and subsequent work showed that light has angular momentum and can impart torque. However, relatively little use has been made of optical forces in applications, the recent commercialization of high-power laser tweezer concepts being a notable exception. Nanophotonic principles have led to devices that offer large fields, such as in the presence of metals, sparking our interest in optical forces over these length scales. In particular, resonances in various forms have played a role in achieving field enhancement that becomes useful in source and detector device functions, and provides an increased Raman or fluorescence dipole moment that promotes sensitive detection of trapped molecules. This background, some of which relate to our contributions, sets the stage for our project.

Our background theoretical work suggests that the Einstein-Laub force density expression can explain all current optical force experiment results when describing total force or pressure. Two important experiments in this regard were the 1978 Jones and Leslie mirror experiment and the 1973 Ashkin and Dziedzic water experiment. Lacking is specific force density data that can be used to establish a predictive theory for design. This can be interpreted as a need for a combined nanometer-scale force experiment and model development or confirmation effort. A lack of such a rigorous combined theoretical and experimental effort to address the physics of optomechanics has hampered optomechanics and the exploitation of the mechanical aspects of light and, more generally, electromagnetics. The goal of this project is to fill this fundamental need in physics, and to draw upon our understanding developed over recent years to present applications that make use of metamaterials and nano-structured materials. Specifically, this project is addressing force theory and modeling and encompasses experimental studies.

2 Introduction

Tweezers: Since the invention of optical tweezers in the 1980s [1], optical manipulation has become important in biology, physical chemistry, and soft condensed matter physics [2]. Forces exerted by a strongly focused beam of light trap small objects. The range of forces realizable [2–8] are ideal for biological and macromolecular systems research [9–11]. In addition, the ability to transport and modify biological entities precisely [12] has led to clinical applications in *in vitro* fertilization [13]. In the physical sciences, it has led to surprising findings in classical statistical mechanics [14], including anomalous attraction [15], oscillatory colloidal interactions [16–19], and hydrodynamic fluctuations [20]. Extending optical trapping down to the nanometer scale would open unprecedented opportunities, allowing accurate positioning of single nano-objects. Recent realizations made use of highly concentrated surface plasmon resonances, concentrating light well beyond the diffraction limit [21], creating a complex near-field landscape and a large number of traps [22]. Plasmonic nanotweezers may play a key role in future integrated analytical platforms, i.e., "lab-on-a-chip." They could complement current microfluidics technology, trapping a single cell for inspection, and could benefit quantum optics research with accurate positioning of cold atoms. These and other important potential applications of nano-optical tweezers have been discussed [21]. Our project involves study of the nanometer-scale optical force, useful in tweezing applications including those depicted in Fig. 1. The work with optical forces may also prove useful in the study of mechanotransduction, or the processes by which cells convert mechanical stimuli into chemical or electrical signals. Perturbations to these signals may disrupt tensional homeostatis, and can lead to diseases such as cardiovascular disease or cancer [23]. To study these forces, very precise control of the applied force is required [24], which is possible using optical forces.

The desire for higher resolution and greater optical force has led to the design of smaller optical

traps. Intrinsically, it is interesting to manipulate/observe nanoparticles, so work was initiated at smaller length scales [25]. However, a Gaussian-focused laser beam can only be focused to a certain extent. Unsurprisingly, alternatives have been sought for increasing the field intensity on much smaller length scales. This has led to the use of nanostructures and plasmonics to apply optical forces and, in some instances, to the creation of nano-optical tweezers [21]. There have also been investigations for forces in waveguides [26] and coupled structures [27, 28]. Gold nanostructures have been formed for the purpose of trapping particles ranging from tens of nanometers to a few microns in radius. Such arrays can be comprised of coupled pairs of nanodots [29], radially large, but very thin microdisks [30], bowtie nanoantennas [31, 32], or dipole nanoantennas [33]. One group fabricated Au nanopillars and tweezed particles around its periphery, rotating the said particles by rotating the polarization of the incident illumination [34]. Despite this progress, a more intimate understanding of the details associated with the optical forces generated by nanostructures is essential for the development/design of new structures for the application of this incredible technology in the future. This goal was pursued during the project.

Radiation Pressure: Radiation pressure is related to a change in momentum (between incident and emitted photons), and it was first measured for a silver mirror more than one century ago [35]. There has been substantial attention given to models (see, for example, [36–41]), but some important issues remain. A key dilemma has been the determination of a satisfactory model, or perhaps more explicitly, the correct interpretation of an existing model, to explain the measured dependence of the force on the background refractive index in experiments by Jones and Leslie [42], which follow earlier work by Jones and Richards [43]. Explaining the Jones and Leslie experiments [42] has become tantamount to resolving whether to use the Abraham [44, 45] or Minkowski [46, 47] momentum forms. Jones [48] presents a nice historical summary of various contributions, making the point that prediction of force experiments is the requirement of any theory. Thus far, there has not been an adequate explanation for the Jones and Leslie experiments, beyond the apparent consistency with the canonical momentum [49]. Associating the Abraham form of the electromagnetic momentum ($\mathbf{E}\times\mathbf{H}/c^2$, with c the speed of light in vacuum) with the electromagnetic energy in nondispersive media yields the single photon momentum magnitude of $\hbar k_0/n$, where n is refractive index, $\hbar = h/2\pi$, with h being Planck's constant, and k_0 is the free space wave number. Doing likewise with the Minkowski momentum ($\mathbf{D}\times\mathbf{B}$) gives a momentum of $n\hbar k_0$. Atoms have been measured to have a recoil momentum of $n\hbar k_0$ [50], important in atom interferometry with optical gratings and consistent with the de Broglie momentum.

We explained the 1978 experiments by Jones and Leslie, showing that the radiation pressure on a mirror depends on the background medium refractive index, using a force model [51]. Those experimental results were predicted for the first time using a force representation that incorporates the Abraham momentum by utilizing the power calibration method employed in the Jones and

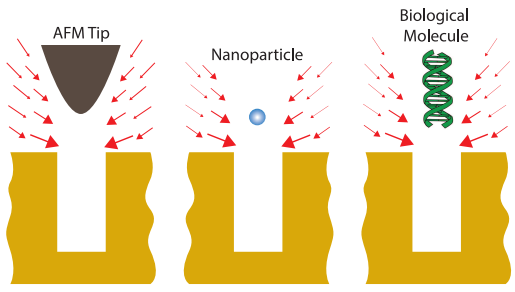

Figure 1. Illustration of the optical nanotweezer function in three situations: (a) atomic force microscope (AFM) characterization experiments; (b) trapping of nanoparticles; and (c) trapping and controlling biological molecules - DNA, molecular motors, or as would apply in mechanotransduction studies of cells. The yellow region is metal (Au), and the 2D and 3D cavities of various shapes can extend through the metal film on a quartz substrate.

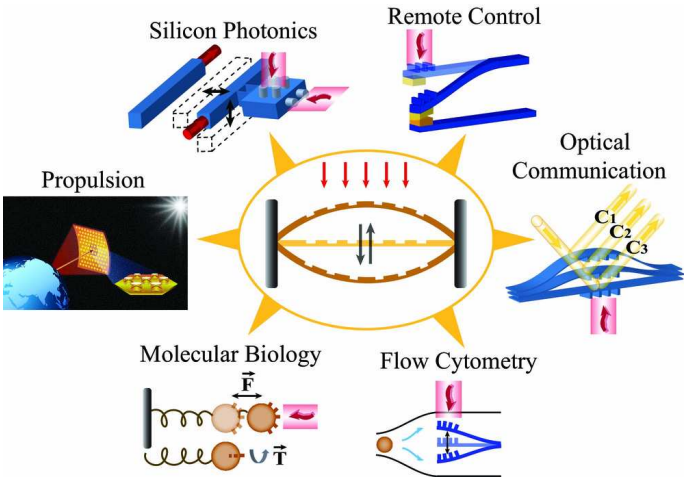

Figure 2. Example application space for a nanostructured surface. The central figure presents the pushing and pulling concept from a incident plane wave (red arrows) in the way of direction control (black arrows). The satellite figures shows the potential applications of optical communication, silicon photonics, and propulsion.

Leslie experiments. Extending the same procedure, the polarization and angle independence of the experimental data was also explained by this model. We also proposed that the pressure on a surface could be increased beyond that on a perfect mirror through control of the nanostructure [52]. The concept and a suite of applications is illustrated in Fig. 2. The center figure shows nanostructured material with a force imparted by plane wave incident from single direction can experience a pushing force (in the direction of incident light) or a pulling force (in the opposite direction), depending on the variables. The satellite images portray a variety of applications. This project involves the physics of optical pressure control with nanostructured material, with impact in applications such as those depicted in Fig. 2.

3 Optical Pressure Theory

3.1 Summary

We present background information on optical pressure obtained as an integral of force density throughout material.

3.2 Kinetic Optical Force Density Leading to Pressure

We utilized the Einstein and Laub force density in material [53], as we have in our previous work [54–57], and as used by others [36, 58]. Using this description, the electromagnetic kinetic force density in material media becomes

$$\mathbf{f} = \frac{\partial \mathbf{P}}{\partial t} \times \mu_0 \mathbf{H} - \frac{\partial \mu_0 \mathbf{M}}{\partial t} \times \epsilon_0 \mathbf{E} + \rho \mathbf{E} - \mu_0 \mathbf{H} \times \mathbf{J} + (\mathbf{P} \cdot \nabla)\mathbf{E} + \mu_0 (\mathbf{M} \cdot \nabla)\mathbf{H}, \tag{1}$$

with $\mathbf{f}$ having SI units of $\mathrm{N/m^3}$ and $\mathbf{P}$ the polarization, $\mathbf{M}$ the magnetization, $\mathbf{J}$ the free electric current density, ρ the free electric charge density, ϵ_0 the permittivity of free space, and μ_0 the permeability of free space. In our special case, the free current and free charge densities will both be zero, and we also assume there is no magnetic material response, so the terms involving $\mathbf{M}$ in (1) are zero. Consequently, one term in (1) describes the radiation pressure, $\partial \mathbf{P}/\partial t \times \mu_0 \mathbf{H}$, and one the gradient force, $(\mathbf{P} \cdot \nabla)\mathbf{E}$. Our interest here is the force that can be exerted on a structured metal surface by laser light, and from (1), the force density within the non-magnetic metal becomes

$$\mathbf{f} = \frac{\partial \mathbf{P}}{\partial t} \times \mu_0 \mathbf{H} + (\mathbf{P} \cdot \nabla)\mathbf{E}. \tag{2}$$

We consider a time-harmonic, monochromatic field with frequency dependence $\exp(-i\omega t)$ and an isotropic dielectric response, giving $\mathbf{P}(\mathbf{r},\omega) = \epsilon_0\chi_E(\mathbf{r},\omega)\mathbf{E}(\mathbf{r},\omega)$, with χ_E the complex electric susceptibility (and dielectric constant $\epsilon = 1 + \chi_E$). With the frequency domain implied, the polarization can then be written as

$$\mathbf{P}(\mathbf{r},t) = \hat{\mathbf{e}}\frac{\epsilon_0}{2}[\chi_E(\mathbf{r})E(\mathbf{r})e^{-i\omega t} + \text{c.c.}], \tag{3}$$

where $\hat{\mathbf{e}}$ is a unit vector, E is the phasor electric field, and c.c. represents the complex conjugate of the first term inside the brackets. By defining $\mathbf{E}$ and $\mathbf{H}$ similarly, the time average of the force density in (2) becomes

$$\langle\mathbf{f}\rangle = (\hat{\mathbf{e}}\times\hat{\mathbf{h}})\frac{\mu_0\epsilon_0\omega}{2}\Im\{\chi_E E(\mathbf{r})H^*(\mathbf{r})\} + \frac{\epsilon_0}{2}\Re\{(\chi_E E(\mathbf{r})\hat{\mathbf{e}}\cdot\nabla)(\hat{\mathbf{e}}E^*(\mathbf{r}))\}, \tag{4}$$

where $\Re\{\cdot\}$ is the real part and $\Im\{\cdot\}$ is the imaginary part. Following a numerical solution for the fields, we use (4) to obtain the time-averaged force density, and then form the pressure by integrating the force density over the appropriate physical dimensions and then dividing by the relevant area.

Consider the simple approximation where the planar Au surface is treated as a perfect electric conductor (PEC), which assumes that the imaginary part of the dielectric constant approaches minus infinity or, equivalently, that the real part approaches plus infinity. Consequently, the skin depth goes to zero and the total field in the incident half-space has zero tangential electric field and a maximum in the magnetic field. The radiation pressure on this surface becomes

$$\langle p_y\rangle = \frac{2S_{-y}k}{\omega} = \frac{2S_{-y}}{c}, \tag{5}$$

where S_{-y} is the incident power density (Poynting vector magnitude in the $-\hat{y}$-direction), k is the (free space, in this case) wave number, and c is the speed of light in vacuum. Equation (5) serves as a reference. This is entirely consistent in the appropriate limit with the classical picture from Maxwell [59], where with a free space background the pressure is

$$P = \frac{S(1+|\Gamma|^2)}{c}, \tag{6}$$

where Γ is the field reflection coefficient at the mirror, S is the time-averaged Poynting vector magnitude (the incident time-average power density), and c is the speed of light.

We summarize the original idea for enhanced pressure devices, where the force density inside the material is integrated [52]. Consider the structured Au metal films in Fig. 3 with free space above and below. A 2D numerical finite element method (FEM) solution [60] for the fields used periodic boundary conditions on the left and right and assumed a plane wave normally incident from above with E_x, H_z (note the coordinate system in the lower left of each figure). The top and bottom surfaces of the simulation domain were implemented as port boundaries so that the scattered waves are absorbed to simulate semi-infinite domains. A wavelength of 632.8 nm was used and the complex dielectric constant for Au was taken from the literature [61]. With the polarization considered, plasmonic cavity modes can form in the slot [62]. We analyzed a number of structures to evaluate the influence of a nanostructured surface on the optical force experienced by the sample. In order to consider a situation representative of an experiment, the Poynting vector of the incident plane wave was normalized for an illumination power density equivalent to 1 mW over a uniformly illuminated circular spot size of diameter 1 μm. We calculated the average force density from (4) using the numerical solutions for the fields for slot widths (W) of 30 nm and 60 nm, and a sequence of depths (D), and upon integration over the thickness of the film, found the pressure on the Au

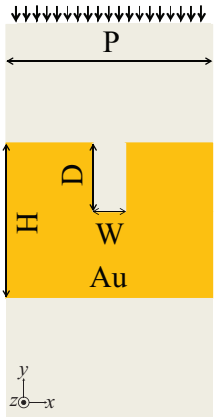

Figure 3. Simulated gold (Au) metal film structures in free space: D is varied between 1 nm and 90 nm, with W set to 30 nm and 60 nm. In all cases, the Au sample is illuminated from the top by 632.8 nm light (E_x, H_z), P is 400 nm, H is 200 nm. Periodic boundary conditions are enforced on the left and right, are port boundaries are on the top and bottom.

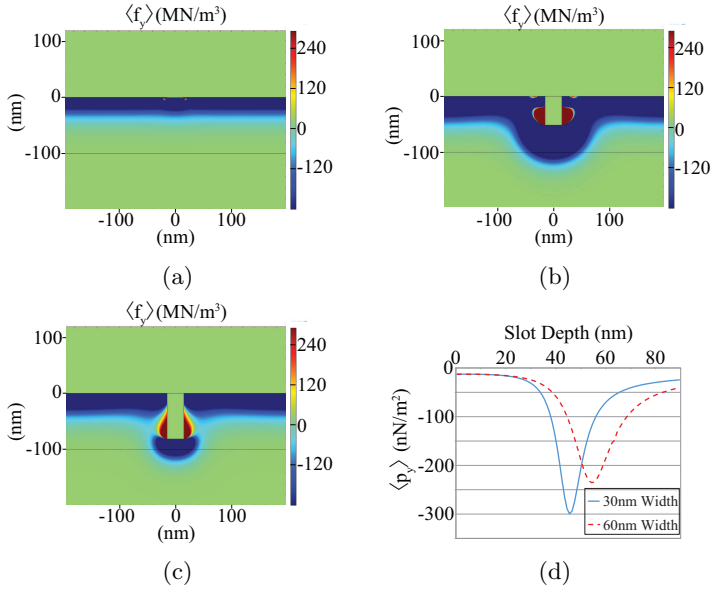

Figure 4. The $y-$component of the force density for the 30 nm wide slot at various slot depths: (a) 1 nm; (b) 51 nm: (c) 81 nm. The simulation has an incident power density equivalent to 1 mW of 632.8 nm laser illumination over a circular spot of diameter 1 μm. For reference, resonance is achieved at about 46 nm for the 30 nm wide slot. (d) Numerical results for the pressure as a function of slot depth in a Au film for the two slot widths, calculated for slot depths from 1 nm to 90 nm in 1 nm steps and $\langle p_y \rangle$, in N/m^2 determined by integrating the $y-$component of force density over the depth of the Au nanostructure. These values are normalized to a Poynting vector power density of 1 W/m^2 and the wavelength is 632.8 nm.

film, $\langle p_y \rangle$. Plots of the $y-$component of force density, $\langle f_y \rangle$, are given in Fig. 4 for a 30 nm wide slot and slot depths of 1, 51, and 81 nm. Notice that the force distribution varies considerably as a function of slot depth. In order to develop a better picture of the relative force enhancement as a function of slot geometry, Fig. 4(d) gives the pressure, $\langle p_y \rangle$, for the 30 nm and 60 nm slot widths as a function of slot depth with a (normalized) input power density of 1 W/m^2. The maximum pressure occurs at the resonant depth, and the peak pressure is higher for the 30 nm slot case. The resonant 30 nm slot in Au at 632.8 nm results in approximately an order of magnitude enhancement in pressure.

As a reference, we simulated the same plane wave incident on the planar Au surface, as shown in Fig. 5(a). The corresponding electric field solution and y-directed force density are plotted in Figs. 5(b) and (c), respectively. Gold can be treated as a very good reflective mirror because of its large reflectivity for 1070 nm light. Consequently, we expect a numerical pressure value very close to the one from (5). From Fig. 5(b), we can identify the skin effect. Using the force density result shown in Fig. 5(c), we calculate a pressure of 2.11 N/m^2, very close to the theoretical value on a PEC mirror, 2.12 N/m^2.

4 Relationship Between the Einstein-Laub Electromagnetic Force and the Lorentz Force on Free Charge

4.1 Summary

An electromagnetic force density expression that is consistent with a development attributed to Einstein and Laub appears to be able to describe optical force experiments done to date with ho-

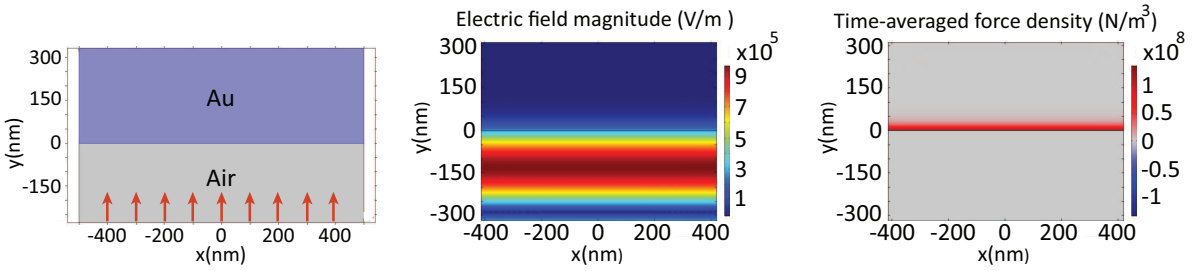

(a) (b) (c)

Figure 5. Simulated field and force density results are shown for a 1070 nm incident plane wave with power density corresponding to a 1 μm radius beam and a power of 1 mW, for a planar Au surface. (a) The geometry for a plane wave illuminating a semi-infinite Au region. (b) Electric field solution for the semi-infinite Au case. (c) y-directed time-averaged force density for the semi-infinite Au case. The point of the simulation is to verify the force model of (4) by agreement with the theoretical value from (5).

mogenized media. However, a major question that has persisted for about one century relates to the apparent discrepancy with the usual interpretation of the force description due to Lorentz in magnetized media. Specifically, it had appeared that the Einstein and Laub force density incorporated only the free space permeability in relation to the force on the electric current density. It is shown here for what appears to be the first time that the Einstein and Laub force density is consistent with the Lorentz picture in the static limit. This resolves a key impediment in establishing a unified force density description for electromagnetic waves interacting with matter. This work has been published in Physical Review B [63].

4.2 Obtaining the Lorentz Force from the Einstein-Laub Force

Understanding the force due to electromagnetic fields is fundamental and of importance in applications like optical tweezers [2, 64] and the study of optical traps [50]. Consequently, the pertinent theory has received substantial attention during the past century (see, for example, [36, 38–41, 53, 53, 55, 65–76]). However, a key and apparently open question has been the description of the electromagnetic force density in magnetic media [36]. In particular, the theory attributed to Einstein and Laub [53], used to explain important experiments [51, 58], has appeared inconsistent with the description due to Lorentz [65] in magnetized media, which is supported by experiments done by Hall [77] and work on electron beams in magnetized media [78, 79]. It is shown here, evidently for the first time, that the Einstein and Laub theory is consistent with that of Lorentz in magnetized media in the static limit, thereby providing a unified description of the force density in homogenized media.

The Lorentz force density (N/m^3) is commonly written as

$$\mathbf{f}_L = \rho\mathbf{E} + \mathbf{J} \times \mathbf{B}, \tag{7}$$

where ρ (C/m^3) is the free electric charge density, $\mathbf{E}$ (V/m) is the electric field intensity, $\mathbf{J}$ (A/m^2) is the electric current density, and $\mathbf{B}$ (T=Wb/m^2) is the magnetic flux density. Equation (7) stems from a static picture of stationary charges and steady state currents. It has no information related to photon momentum or the wave character of light, although of course an electromagnetic wave can establish a charge density and a current density in a material.

A focus of Lorentz was on charges moving in vacuum [65], where in (7)

$$\mathbf{B} \;=\; \mu_0\mathbf{H}, \tag{8}$$

with μ_0 (H/m) the free space permeability and $\mathbf{H}$ (A/m) the magnetic field intensity. However, in homogenized magnetic media having magnetization $\mathbf{M}$ (A/m), one has [80]

$$\mathbf{B} \;=\; \mu_0(\mathbf{H} + \mathbf{M}). \tag{9}$$

Early evidence for the use of (9) in (7) came from the resistivity experiments of Hall in ferromagnetic media, and he provided an explanation in terms of magnetization [77]. This has been understood as a spin-orbit effect and described with $\mathbf{H}$ and $\mathbf{M}$ contributions [81]. The related anomalous Hall effect is the subject of substantial recent interest [82]. While some experiments gave conflicting pictures [83] (see the introduction), a result showing the deflection of mesons by magnetized iron also suggested that use of (9) in (7) is correct [83]. Electron microscopy has been used to determine the distribution of magnetism [84], and those experiments also support use of magnetization ($\mathbf{M}$) in evaluating the force on a beam and indicate that in the situations considered the applied field ($\mathbf{H}$) was unimportant. Subsequent work indicated sensitivity to magnetized material states [78, 79], and the characterization method became known as Lorentz microscopy. Therefore, as is broadly understood, experimental evidence overwhelmingly supports use of (9) in (7). This established background is projected against an apparent discrepancy with a rigorous theory for the electromagnetic force density that presumably should approach (7) in the static limit.

The particular challenge of relevance here has been that $\mathbf{J}\times\mu_0\mathbf{H}$ appears in the electromagnetic force density attributed to Einstein and Laub [53], and the explanation has presented an open issue for a very long time (see, for example, [36, 85]). It is shown here that in fact the Einstein and Laub force density expression is in agreement with Lorentz and (7) together with (9) in the static limit.

The force density attributed to Einstein and Laub [53] ($\mathbf{f}_{EL}$ N/m^3) and used by many [36, 54, 55, 68, 71–73, 76] is

$$\begin{aligned}\mathbf{f}_{EL} &= \frac{\partial\mathbf{P}}{\partial t}\times\mu_0\mathbf{H}-\frac{\partial\mu_0\mathbf{M}}{\partial t}\times\epsilon_0\mathbf{E}\\ &\quad+\rho\mathbf{E}+\mathbf{J}\times\mu_0\mathbf{H}+(\mathbf{P}\cdot\nabla)\,\mathbf{E}+\mu_0\,(\mathbf{M}\cdot\nabla)\,\mathbf{H},\end{aligned}\tag{10}$$

where $\mathbf{P}$ (C/m^2) is the polarization and ϵ_0 (F/m) is the free space permittivity. The corresponding stress tensor is [51]

$$\mathbf{T}_{EL}=\frac{1}{2}\left(\epsilon_0E^2+\mu_0H^2\right)\mathbf{I}-\mathbf{DE}-\mathbf{BH},\tag{11}$$

where $\mathbf{I}$ is the identity matrix, $\mathbf{D}$ (C/m^2) is the electric flux density, and, for example, $\mathbf{DE}$ is a dyadic product of two vectors with elements $(\mathbf{ab})_{ij}=a_ib_j$ [36]. This stress tensor is arrived at through incorporation of coupled electromagnetic, polarization, and magnetization systems [51]. For general material arrangements, $(\mathbf{P}\cdot\nabla)\mathbf{E}$ and $(\mathbf{M}\cdot\nabla)\mathbf{H}$ in (10) can be nonzero, and the identities

$$-(\nabla\cdot\mathbf{P})\,\mathbf{E} = -\nabla\cdot(\mathbf{PE})+(\mathbf{P}\cdot\nabla)\,\mathbf{E}\tag{12}$$

$$-(\nabla\cdot\mathbf{M})\,\mathbf{H} = -\nabla\cdot(\mathbf{MH})+(\mathbf{M}\cdot\nabla)\,\mathbf{H}\tag{13}$$

indicate that $\mathbf{PE}$ and $\mathbf{MH}$ provide a contribution in (11).

In vacuum and for the static limit, (10) produces $\rho\mathbf{E}+\mathbf{J}\times\mu_0\mathbf{H}$, the Lorentz result in (7), providing confidence. The relevant point related to the credibility of (10) addressed here is the static limit in magnetic materials, and consistency with the work of Lorentz (7). Equation (10) has $\mathbf{J}\times\mu_\mathbf{0}\mathbf{H}$, while static experiments suggest that it should be $\mathbf{J}\times\mathbf{B}$. Introducing an electron beam into a sample, where we make the assumption of uniform velocity, would appear to be captured in $\mathbf{J}$. Therefore, at least superficially, there appears to be an issue with consistency between (10) and (7). It has earlier been proposed that the root of the issue is that (10) applies to local, homogenized media, and the situation of charges passing through material is more complicated and may not conform [36]. However, $\mathbf{J}$ can be viewed as an impressed current (a mathematical source) that can encompass Ohm's law and the steady current when $\partial\mathbf{P}/\partial t\to 0$, or is an equivalent current (in the Huygen's sense). A legitimate electromagnetic force theory should capture this as the circular temporal frequency (ω) approaches zero, i.e., in the static limit. Therefore, consider more carefully the static limit for (10), where terms involving a time derivative are removed.

Use of the identity $(\nabla \mathbf{b}) \cdot \mathbf{a} = (\mathbf{a} \cdot \nabla)\mathbf{b} + \mathbf{a} \times (\nabla \times \mathbf{b})$ with tensor operation $(\nabla \mathbf{b})_{ij} = \partial b_j / \partial x_i$, gives

$$(\nabla \mathbf{H}) \cdot \mathbf{M} = (\mathbf{M} \cdot \nabla)\mathbf{H} + \mathbf{M} \times (\nabla \times \mathbf{H}). \tag{14}$$

Using (14), and with reference to (10),

$$\begin{aligned} \mu_0(\mathbf{M} \cdot \nabla)\mathbf{H} &= \mu_0(\nabla \mathbf{H}) \cdot \mathbf{M} - \mu_0 \mathbf{M} \times (\nabla \times \mathbf{H}) \\ &= \mu_0(\nabla \mathbf{H}) \cdot \mathbf{M} + \mathbf{J} \times \mu_0 \mathbf{M}, \end{aligned} \tag{15}$$

with application of Ampere's law for magnetostatics, neglecting displacement current (to investigate the relationship between (10) for the *static case* and the Lorentz result). With (15), and considering the two relevant terms in (10),

$$\begin{aligned} \mathbf{J} \times \mu_0 \mathbf{H} + \mu_0(\mathbf{M} \cdot \nabla)\mathbf{H} &= \mathbf{J} \times \mu_0 \mathbf{H} + \mu_0(\nabla \mathbf{H}) \cdot \mathbf{M} + \mathbf{J} \times \mu_0 \mathbf{M} \\ &= \mathbf{J} \times \mathbf{B} + \mu_0(\nabla \mathbf{H}) \cdot \mathbf{M} \\ &= \mathbf{J} \times \mathbf{B}, \end{aligned} \tag{16}$$

where the approximation assumes that the local, mean field is constant over the length scale of interest ($\nabla \mathbf{H} = 0$), appropriate because this is a force density. The force density here is a macroscopic quantity and is applicable with spatial averages (mean field) over a length scale appreciable relative to inter-atomic distances [86, 87]. The assumption of a constant local field is also compatible with the local homogenization of materials [87] (and a more recent example from metamaterials [88]). Equation (16) indicates that (10) is consistent with the result from Lorentz for the static force on a free current density $\mathbf{J}$, expressed in (7). This key point does not seem to have been recognized previously.

Consider now the electrostatic situation. Using the same vector identity that led to (14),

$$\begin{aligned} (\nabla \mathbf{E}) \cdot \mathbf{P} &= (\mathbf{P} \cdot \nabla)\mathbf{E} + \mathbf{P} \times (\nabla \times \mathbf{E}) \\ &= (\mathbf{P} \cdot \nabla)\mathbf{E} \\ &= 0, \end{aligned} \tag{17}$$

because the electrostatic field is conservative and hence has zero curl, and with the assumption of a locally constant field, $\nabla \mathbf{E} = 0$, so from (17), $(\mathbf{P} \cdot \nabla)\mathbf{E} = 0$.

With use of (16) and (17) in (10), and in the static limit,

$$\lim_{\omega \to 0} \mathbf{f}_{EL} = \rho \mathbf{E} + \mathbf{J} \times \mathbf{B} = \mathbf{f}_L, \tag{18}$$

in agreement with (7). Equation (18), showing the force density on a free charge distribution, is the central result. Using $\nabla \mathbf{H} = 0$ and $\nabla \mathbf{E} = 0$, introduced here for the first time, (18) can be obtained from a previous development based on (10) [85].

In part, the point of this Letter is to draw attention to the meaning of the terms in (10) in relation to the material properties and the force description in (7) due to Lorentz. This has been considered a major problem, i.e., that there is not an adequate picture linking the two forms [36, 85]. An electric current source or an equivalent boundary representation is captured by $\mathbf{J}$ in (10). Free and bound charge motion are rigorously incorporated in a temporal Fourier representation of $\mathbf{P}(t)$ and $\mathbf{M}(t)$ in (10), so in a simple isotropic situation the complex susceptibilities provide the complete material description: $\mathbf{P}(\omega) = \epsilon_0(\chi'_E + i\chi''_E)\mathbf{E}(\omega)$ and $\mathbf{M}(\omega) = (\chi'_H + i\chi''_H)\mathbf{H}(\omega)$. Taking (10) into the frequency domain, we can legitimately represent the complex electric susceptibility as a complex conductivity ($\sigma = \sigma' + i\sigma''$), thereby forming the equivalence between $\partial \mathbf{P}/\partial t \times \mu_0 \mathbf{H}$ and $\mathbf{J} \times \mu_0 \mathbf{H}$.

For a locally homogeneous medium, the fields are divergenceless (so for the isotropic material case, $\nabla \cdot \mathbf{E} = 0$ and $\nabla \cdot \mathbf{H} = 0$) and a plane wave superposition can be used. In this situation, the "free charge" density within the material is $\nabla \cdot \mathbf{D} = \rho = 0$. Current density and charge density are of course linked through the conservation of charge requirement in the continuity condition. In the static case, $\mathbf{J}$ describes the conduction current density (free charge) and $\mathbf{P}$ the bound charge, and the two terms can be separated exactly. In the context of homogeneous media, $\mathbf{J}$ and ρ in (10) describe the free or introduced charged particles, the e-beam for instance. This is precisely the framework to understand how (10) maps to (7).

Let us review what $\nabla\mathbf{H} = 0$ and $\nabla\mathbf{E} = 0$ in (16) and (17) means in the broader physical context in arriving at (18). First, the obvious statement that $\nabla\mathbf{H}$ and $\nabla\mathbf{E}$ do not appear in (7), either because only the local field is relevant (and not its spatial variation at each point in space) or something has been ignored, perhaps electrostriction and magnetostriction, in applying (7) in materials. The fact that an enormous body of experimental work in dielectric and magnetic materials with static fields supports (7) suggests that it captures the relevant physics thus far. The issue then becomes the basis of any approximation. The case was made that the mean, local field that is built into Maxwell's equations implies that only the field amplitude, and not the spatial variation, should be used in the force density impacting free charge motion in a material. For a linear time-invariant problem, superposition can be applied. Each elemental component of the beam has weights $\mathbf{J}(\mathbf{r}')$ and $\rho(\mathbf{r}')$ at some point $\mathbf{r} = \mathbf{r}'$ in space. Thus, an element of the current density is $\mathbf{J} = \hat{\mathbf{j}} J(\mathbf{r}')\delta(\mathbf{r} - \mathbf{r}')$, where $\hat{\mathbf{j}}$ is a unit vector and $\delta(\cdot)$ is the Dirac delta function. In this mathematical Dirac limit and a point-wise spatial representation, clearly $\nabla\mathbf{H} = 0$ and $\nabla\mathbf{E} = 0$ at each point where the force (density) on the charged particle beam is determined, considering the differential limit for a continuous field. Integration over a differential volume gives the local force on the current and charge.

Consider again the physical picture behind (18). The description is of the force on free charge (the e-beam for instance) in a material. It is not the force deforming the material. In this sense, electrostriction and magnetostriction are irrelevant. Earlier work considering the relationship between the Lorentz and Einstein-Laub forces (see [58, 85], for example), considered the force on the material rather than directly considering the force on the free charge density. Hall measurements monitor current and hence conform to this picture. Although straight forward, this point is important because it allows the decomposition of the Einstein-Laub force into a form that is exactly equivalent to the Lorentz picture, as widely used and as it must.

4.3 Conclusion

Equation (18) indicates that the Einstein-Laub formulation for force density is consistent with the accepted static form of the Lorentz force on free charges in static fields. This means that the material magnetization will influence the local force density in (10), just as in the expression from Lorentz that has been supported by experiments. Equation (10) has been used to explain key optical force experiments, including those due to Jones and Leslie [42] (see [51]), as well as Ashkin and Dziedzic [89] (see [58]). It might optimistically be concluded that legitimate interpretations of (10) may be able to explain all macroscopic experiments. Whether other theories hold, at least approximately, in certain situations represents another set of questions. Finally, lacking in force experiments has been verification of the influence of the dispersive material response that is incorporated into (10) through $\partial\mathbf{P}/\partial t$ and $\partial\mu_0\mathbf{M}/\partial t$.

5 Enhanced Optical Pressure with Asymmetric Cavities

5.1 Summary

Asymmetry in an optical cavity is investigated as a basis for enhanced pressure [90] to develop understanding of experimental results with nanostructured membranes where surface plasmon modes exits [91].

5.2 Background

Cavity dynamics concepts are based on the mirror radiation pressure being $P = 2\hbar k I$, with each photon carrying a momentum $\hbar k$ and I being the optical intensity measured in photons/(m^{2}s), given P in N/m^2, and the factor of two is from the assumption of perfect reflection [92]. This is entirely consistent in the appropriate limit with the classical picture from Maxwell [59], given in (6). Clearly, increasing I or the Poynting vector within the cavity by increasing the cavity quality factor (Q) will increase the pressure on each mirror. However, $|\Gamma| = 1$ leads to a maximum value of $P = 2S/c$ in this widely-held picture.

The force density in homogenized media can be obtained from the field solution, and this leads to a means to calculate the force on a medium [58, 93], the pressure on a slab [57, 94], and with photonic crystal mirrors [95]. With such an approach involving a numerical solution for the fields in the material, leading to the force density and hence pressure, the possibility of increasing the pressure by more than an order of magnitude over $2S/c$ with a nanostructured Au surface has been presented [52]. This result could be profoundly important in applications, but the physical basis of the effect has remained unclear. Here, we present an understanding based on results for an asymmetric cavity. This metal-insulator-metal (MIM) cavity mode basis leads to a means to achieve pressure enhancement with a variety of dielectric and metallic materials for remote control, propulsion, and cavity optomechanics applications. The resulting change in the mathematical picture of pressure [59] should therefore provide a basis for new directions in optomechanics for the physical sciences.

We consider optical pressure enhancement on a surface as a cavity effect by considering symmetry (Figs. 6(a)) and asymmetry (Fig. 6(b)), along with the asymmetric MIM cavities in Figs. 6(c) and (d), all in a free space background. Figure 6(a) shows a symmetric cavity containing two identical slab mirrors (M_1 and M_2) with thickness t, and a cavity length d, defined as the mirror separation. Figure 6(b) shows an asymmetric cavity with M_1 having thickness t and the semi-infinite M_2 placed a distance d away from M_1. Figure 6(c) shows a nanostructured slot cavity array in metal and the profile of each slot is shown in Fig. 6(d). With an incident field having H_z, the lowest order MIM waveguide mode (E_x, E_y, H_z) can be excited, by virtue of the metal dielectric constant ($\epsilon = \epsilon' + i\epsilon''$ with $\epsilon' < -1$, assuming a free space background) [96]. The coupled surface plasmon waveguide mode has a wavelength that reduces with decreasing slot width (Σ), allowing for resonant cavities in gold (Au) where the slot depth (D) and Σ are just a few tens of nanometers. The cavity in Fig. 6(d) has differing reflection coefficients at the top and bottom of the slot, resulting in asymmetry.

5.3 Asymmetric Cavity Pressure

The force density expression we utilize here, originally from Einstein and Laub [53], has been derived and used by others [36, 57, 58, 93], and was also used to present the idea of enhanced pressure in structured material [52]. We assume that no magnetic material response exists in the source-free case. Consequently, the time-averaged force density within the material media assuming $\exp(-i\omega t)$ is

$$\begin{aligned} \langle \mathbf{f} \rangle &= (\hat{\mathbf{e}} \times \hat{\mathbf{h}}) \frac{\mu_0 \epsilon_0 \omega}{2} \Im\{\chi_E E(\mathbf{r}) H^*(\mathbf{r})\} + \frac{\epsilon_0}{2} \Re\{(\chi_E E(\mathbf{r}) \hat{\mathbf{e}} \cdot \nabla)(\hat{\mathbf{e}} E^*(\mathbf{r}))\} \\ &= \langle \mathbf{f}_{\mathrm{R}} \rangle + \langle \mathbf{f}_{\mathrm{G}} \rangle, \end{aligned} \tag{19}$$

where $\hat{\mathbf{e}}$ and $\hat{\mathbf{h}}$ are unit vectors indicating the direction of the electric and magnetic field phasors, E and H, at position $\mathbf{r}$, respectively, χ_E is the electric susceptibility, $\Re\{\cdot\}$ is the real part and $\Im\{\cdot\}$ the imaginary part, μ_0 is the free space permeability, and ϵ_0 is the free space permittivity. We define the time-averaged force density due to the first term in (19) as $\langle \mathbf{f}_{\mathrm{R}} \rangle$, where the nomenclature implies that this is the radiation pressure for a planar surface with normal incidence, the usual mirror picture, and the other term due to the gradient of the field as $\langle \mathbf{f}_{\mathrm{G}} \rangle$. We note that application

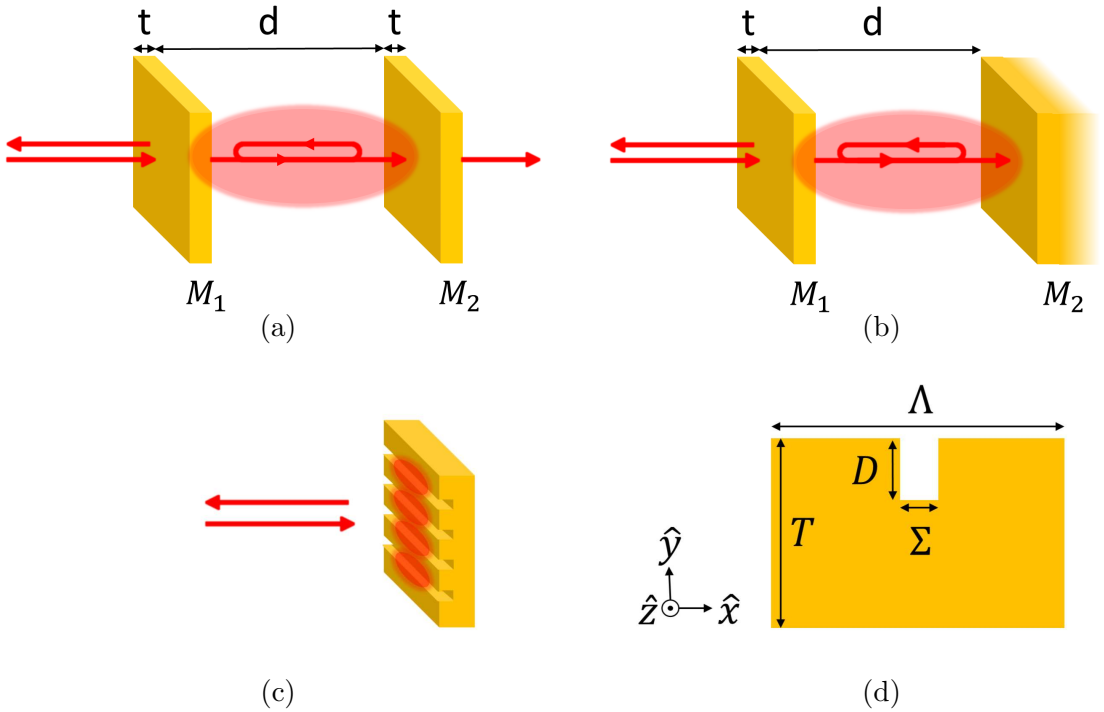

Figure 6. Optical cavities that enhance the radiation pressure. (a) A symmetric Fabry-Perot cavity. The mirrors M_1 and M_2 are two identical slabs with thickness t separated by d. (b) An asymmetric Fabry-Perot cavity. M_1 is a slab with thickness t and M_2 is a semi-infinite mirror placed d away from M_1. (c) A nanostructured slot cavity array in a metal. (d) Profile of the nanostructured slot cavity in (c).

of (19) for normally incident light on a planar Au mirror and integration over depth produces a pressure for visible wavelengths that is very close to $2S/c$. Conservation of momentum is inherent in use of (19) because this kinetic force density is formed with use of the classical field momentum [51, 53, 93].

We relate the radiation pressure to the cavity Q for the MIM cavity in Fig. 6(d). With the linear and isotropic relationships $\mathbf{D} = \epsilon_0\epsilon\mathbf{E}$ and $\mathbf{B} = \mu_0\mathbf{H}$, in frequency domain and where $\mathbf{D}$ is the electric flux density and $\mathbf{B}$ the magnetic flux density, it is possible to separate electromagnetic field energy into stored and lost components [97]. Under the assumption that dispersion can be neglected, so $\partial\epsilon/\partial\omega = 0$, the time-averaged stored energy surface density (J/m^2) is

$$W = \frac{1}{4}\int_l \left[\epsilon'\epsilon_0|E(\mathbf{r})|^2 + \mu_0|H(\mathbf{r})|^2\right] \mathrm{d}l, \tag{20}$$

where l is the spatial variable perpendicular to the mirrors. Likewise, the time-averaged power dissipation surface density (W/m^2) is

$$P_\mathrm{d} = \frac{\omega}{2}\int_l \epsilon_0\epsilon''|E(\mathbf{r})|^2 \mathrm{d}l. \tag{21}$$

The integrations in (20) and (21) are over the mirrors and the intervening space (free space in the situations of Figs. 6(a) and (b)), and for M_2 in the asymmetric cavity case, the integral in that mirror is over 20δ, with δ the skin depth (e^{-1} of the field at the surface).

The Q can be decomposed into unloaded (accounting for loss within the cavity, Q_U) and loaded (describing the radiative loss contribution, Q_L) as

$$\frac{1}{Q} = \frac{1}{Q_\mathrm{U}} + \frac{1}{Q_\mathrm{L}}, \tag{22}$$

where

$$Q_{\rm U} = \omega_0 \frac{W_0}{P_{\rm d}} \quad \text{and} \quad Q_{\rm L} = \omega_0 \frac{W_0}{S_{\rm r} + S_{\rm t}}, \tag{23}$$

with ω_0 the resonant circular frequency, W_0 the total (electric plus magnetic) energy in the cavity at resonance from (20), $P_{\rm d}$ the power dissipated within the cavity at resonance from (21), and $S_{\rm r}$ and $S_{\rm t}$ the reflected and transmitted Poynting vector magnitudes, respectively, at resonance. With high cavity finesse and use of a Lorentzian line model [98, 99],

$$1 - |S_{11}(\omega)|^2 \;\; = \;\; \frac{1 - |S_{11}(\omega_0)|^2}{1 + 4\frac{(\omega_0 - \omega)^2}{\Delta\omega^2}}, \tag{24}$$

and an estimate of Q is

$$Q_\omega = \frac{\omega_0}{\Delta\omega}, \tag{25}$$

where $\Delta\omega$ is the half-power bandwidth and the subscript ω indicates this frequency response measure (with a high Q approximation). Measuring S_{11} and use of (25) to determine Q circumvents the need to artificially define cavity boundaries.

5.4 Pressure with a Slot Array in a Metal Film

To obtain the fields and the corresponding radiation pressure in the nanostructured slot cavity in a metal film, shown in Fig. 6(c), we use a frequency domain finite element method (FEM) to obtain the numerical field solutions [60]. Port boundaries are used in this 2-D model to extract S_{11} and placed $5\lambda_0$ above and below the structure in Fig. 6(d). To avoid singularities in the numerical simulations, the corners of each slot are rounded with radius of 1 nm. The maximum mesh element size in the scattering material is $\lambda_0/200$, sufficient to ensure the accuracy of the force density solutions. The slot depth, D, and width, Σ, are variables and the period is set to $\Lambda = 400$ nm and thickness to $T = 200$ nm. With a period of $\Lambda = 400$ nm, only the zeroth-order (normal) scattered plane wave propagates. We fix Σ and vary D to determine the resonant depth from the minimum of $|S_{11}|$.

The results for the slot resonant D as a function of Σ, labeled by the (red) diamonds, are shown on the right axes in Figs. 7(a) and (b). A reducing slot width results in a decreasing slot depth for the first resonance. We apply (25) to estimate Q_ω for the slot cavity, and the results are shown in Fig. 7(a) by the (black) triangles in conjunction with the left axis. Note that Q_ω increases with decreasing Σ, which can be understood by the cavity reflection coefficient at the top of the slot increasing as Σ is reduced, thereby increasing the lifetime of the guided-wave resonance in the slot and hence Q_L. The numerical field solutions are used in (19) to find the force density, and this is integrated over the support of the material within the unit cell and divided by Λ to form the pressure, with the results given by the (black) asterisks for each value of Σ in Fig. 7(b), as indicated on the left axis. The general trends in Figs. 7(a) and (b) are that both Q_ω and pressure decrease with increasing slot width (at resonance). Figure 7(c) shows the pressure as a function of Q_ω for the slot structures. Unlike the 1D Fabry-Perot cavities, the gradient force term, $\langle \mathbf{f}_{\rm G} \rangle$, contributes. We separate the contribution of $\langle \mathbf{f}_{\rm G} \rangle$ from the total pressure (black asterisks), and the results are plotted as the red circles in Fig. 7(c). In general, the pressure is proportional to Q_ω and the relationship is linear for lower Q_ω. Higher Q_ω supports a higher pressure contribution from $\langle \mathbf{f}_{\rm G} \rangle$, associated with the reducing slot width, although the total pressure reduces slightly at the highest Q_ω. The dashed line is again the maximum pressure on a perfect mirror. The gradient of the total pressure in Fig. 7(c), dP/dQ_ω, describes the efficacy of the cavity in enhancing the pressure (per unit Q or stored energy). In Fig. 7(d), we plot the linear fits passing through the origin for the total pressure and the pressure contributed by $\langle \mathbf{f}_{\rm G} \rangle$ as black and red dashed lines, respectively, using the first 8 points (linear region) in Fig. 7(c).

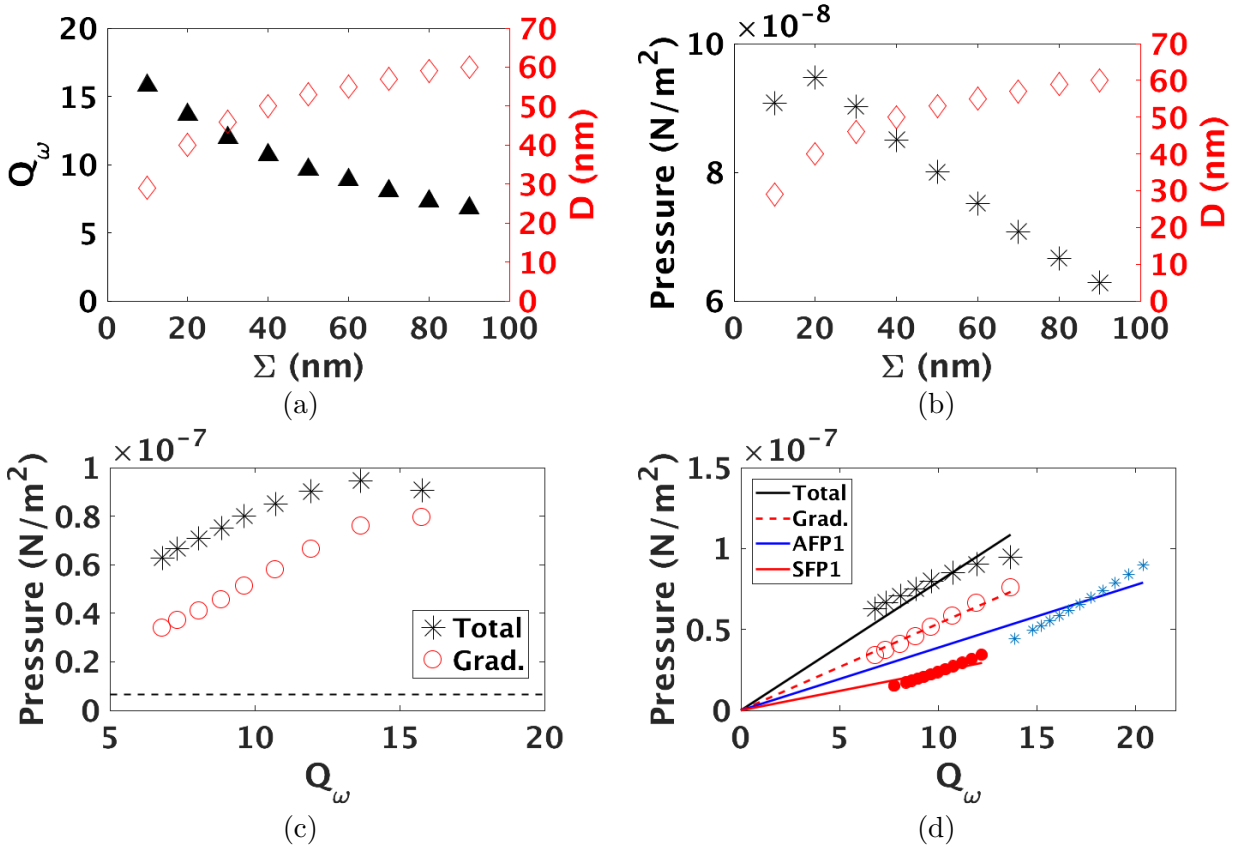

Figure 7. Simulation results for the nanostructured slot cavity array in Au, and with reference to Fig. 6(d): $\Lambda = 400$ nm, $T = 200$ nm, Σ is fixed, and D is varied to determine the resonant depth D from the minimum of $|S_{11}|$. (a) Q_ω (triangles) and resonant slot depth, D (diamonds), as a function of slot width, Σ. (b) Radiation pressure (asterisks) along with the resonant D (diamonds) as a function of Σ. In general, smaller Σ results in higher Q_ω and larger pressure. (c) Radiation pressure as a function of Q_ω, decomposed into total and gradient ($\langle \mathbf{f_G} \rangle$) contributions. The dashed line shows the maximum pressure on a perfect mirror. The nanostructured slot cavity supports a pressure enhancement more than an order of magnitude higher than a perfect mirror. (d) Radiation pressure as a function of Q_ω for lower Q cavities, in comparison with the slot pressures from (c). The black line and red dashed line are the linear fits to the total pressure and $\langle \mathbf{f_G} \rangle$, respectively from the first 8 points in (c). For details, see Ref. [90].

5.5 Conclusion

We have shown that an asymmetric MIM optical cavity can lead to a total pressure as the sum of that on each mirror that exceeds the pressure on a perfect mirror, when considering the force density within the material. This net pressure is substantial by virtue of the asymmetry and can be controlled by cavity Q. The enhanced pressure for the nanostructured metal film results from both terms in (19), where the cavity mode resonance influences the fields in the metal and hence the force density and pressure. Generally, increasing the cavity Q can produce higher pressure in the metal film slot resonators. The kinetic force density in (19) is derived using conservation of momentum (see [93], for example). Consequently, there is a rigorous basis for the pressure results shown. A surface plasmon is excited in the slot cavity, associated with the lowest-order MIM mode that propagates for arbitrarily small slot width, allowing for very small cavities. However, other cavity modes using other materials, including dielectrics, are expected to also provide pressure enhancement. There are convenient fabrication methods to form nanocavity arrays in metal, for example, direct nanoimprinting [100]. With use of optimized, aperiodic structures, more control and higher pressure should be possible [101], and regulation of the pressure as a function of wavelength should be possible. The explanation for enhancement we have provided allows design guidelines for

applications that will benefit from enhanced and controllable optical forces with structured material. For example, beads that are used in optical tweezers could be structured [102]. Also, the efficacy of vehicle propulsion using structured materials should improve. More generally, we suggest that there are new opportunities related to the interaction of waves with structured, resonant materials and the generation of a mechanical response.

6 Optical Forces in Aperiodic Materials

6.1 Summary

The electromagnetic force on matter depends on both the geometry and material properties, and for a contiguous material, the pressure is a useful metric. We present a statistical method with example results that allows the evaluation of pressure in relation to a nanostructured material arrangement. We show that it is possible to obtain a pressure substantially greater than that on a perfect, planar mirror, and relate this to resonant field features. With some material arrangements, the pressure can be negative, and this can again be related to resonances. Negative pressure can be understood as being due to the total field, a superposition of the incident and scattered fields, where the structure regulates the local scattered field and hence the pressure through an integral of the resulting force density. The statistical analysis provides physical insight into how to regulate both the pressure magnitude and direction and hence provides a framework for applications. The fields impacted include biophysics, where information is obtained about biomolecules from force and torque measurements, cavity optomechanics related to basic science and sensing, and optical remote control and actuation, where regulation of the magnitude and direction, and the possibility of materials with multiple functionalities, provides new opportunities. This work has been published in the Journal of the Optical Society of America B [103].

6.2 Background

Aperiodic, irregular structures can provide a large number of degrees of freedom relative to periodic systems and hence the possible more control over electromagnetic fields. Our previous results show that some unintuitive realizations for waveguide [104–109] and diffractive [110] elements can be achieved from aperiodic-structured material to present functions that are not possible with conventional concepts, such as those involved periodic structures. However, few guidelines exist for the design of aperiodic materials. The exploration of the aperiodic material design area can only rely on optimization-based solutions. We recently provided a multivariate statistical analysis of binary aperiodic structures that gives physical understanding of the relationship between structure and electromagnetic field control [101]. The eigen-decomposition of the field covariance matrix provides a measurable number to compare the field variances (σ_C^2) on the detector plane to evaluate the possible degrees of freedom from the aperiodic structured materials in different cases.

Our results have shown that some physical resonances occur when a certain material property or discretization is chosen and this feature has a significant impact on the transmitted energy and the field variance (σ_C^2) [101]. Our previous work [52] and our ongoing research have shown that structured materials can provide a large enhancement of the optical force, relative to that on planar metallic surfaces, due to cavity-enhanced fields and the excitation of surface waves. Based on our experience and understanding related to aperiodic nanostructured materials, we are particularly interested in how the large number of degrees of freedom supported by aperiodic materials may contribute on the control of the optical force.

6.3 Aperiodic Nanostructured Material

Figure 8 shows the 2D geometry of the binary aperiodic nanostructured material we consider. A $\lambda_0 = 633$ nm plane wave is normally incident from the left in free space with $\mathbf{H}$ in the $\hat{\mathbf{z}}$ direction. This incident field is the lowest-order TM_x mode in the parallel plate geometry (the TEM mode). The material structure is defined within a wavelength-sized region (633 nm on a side). This domain is divided into $P \times P$ pixels. Each pixel can be either the scatterer or the background (free space).

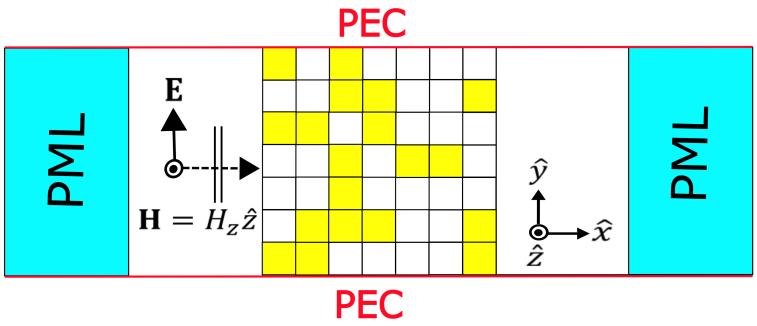

Figure 8. Binary aperiodic nanostructured material simulation geometry: PML, perfectly matched layer; PEC, perfect electric conductor. The width and length of the discretized region is 633 nm. A $\lambda_0 = 633$ nm plane wave with $\mathbf{H}$ in the $\hat{\mathbf{z}}$ direction is normally incident from the left. The binary nanostructured material is divided into $P \times P$ elements and each element is either the scatterer or the background (free space in our case). To avoid singularities in the numerical simulations, the side length of each scatterer is reduced by 1 nm, and the corners are rounded with a radius of 1 nm.

The size and arrangement of the pixels having scattering material has a dramatic impact on optical pressure, as we describe. Fixing the fill factor, f, specifies the number of scatterers. We do this by truncating the number formed from fP^2 to an integer value. To avoid singularities in the numerical simulations, the side of each scatterer is reduced by 1 nm and the corners are rounded with a radius of 1 nm. The maximum mesh element size in the scattering material is $\lambda_0/200$, adequate to support the accuracy of the force density solutions. The top and bottom of the computational domain are bounded by perfect electric conductor (PEC) surfaces to form a waveguide. We apply perfectly matched layers (PMLs) on both the left and right boundaries to simulate unbounded space for the scattered fields. All simulations assume an incident power density of 1 W/m^2.

The pressure is calculated from the integral of $\langle \mathrm{f_x} \rangle = \langle \mathbf{f} \cdot \hat{\mathbf{x}} \rangle$, where $\langle \mathbf{f} \rangle$ is from (4) and the direction of $\hat{\mathbf{x}}$ is shown in Fig. 8, over all scatterers in the aperiodic nanostructure and then divided by the exposed surface (633 nm in our 2D simulations). While the segments of the aperiodic structure are not contiguous, we assume that another material can provide the structure, making the use of pressure meaningful.

6.4 Statistical Field and Pressure Analysis of Aperiodic Structures

We utilize a multivariate statistical method to relate field control (regulation of the scattered field, as a function of position here) and pressure control (the average force magnitude and direction) to the attributes of the binary nanostructures. Consider the transmission matrix, $\mathbf{T}$, defined as

$$\mathbf{T} = \left[\frac{H_u}{H_{iv}}\right], \quad v \in [1, ..., \Upsilon] \quad u \in [1, ..., U], \tag{26}$$

where H_{iv} is the incident (plane wave) magnetic field along points on the constant-x input line (with an absolute position that is unimportant) and H_u is the total field along the output line (and we choose a constant-x line that is $\lambda_0/8$ behind and to the right of the structure). The H_u samples are therefore in the near-field and influenced by both propagating and evanescent fields. In the simulations, we choose $\Upsilon = U = 101$ and divide the input and the output lines (the 633 nm long input and output lines between the two PEC surfaces in Fig. 8) into uniformly spaced points. The $(U \times U)$ field covariance matrix, $\mathbf{C}$, can be calculated as [111]

$$\mathbf{C} = \langle \mathbf{T}^H \mathbf{T} \rangle - \langle \mathbf{T}^H \rangle \langle \mathbf{T} \rangle, \tag{27}$$

where H is Hermitian transpose and $\langle \cdot \rangle$ is the average over all samples. A sample means a particular nanostructured scattering material arrangement, resulting in a specific $\mathbf{T}$.

The variance of $\mathbf{C}$ is defined as [111]

$$\sigma_C^2 = \sum_{u=1}^{U} \sigma_u^2 = \sum_{u=1}^{U} C_{uu} = \mathrm{Tr}\{\mathbf{C}\}, \tag{28}$$

where the C_{uu} are the diagonal elements of $\mathbf{C}$ and $\mathrm{Tr}\{\cdot\}$ is the trace. It can be shown (see, for example, [112] page 264) that

$$\mathrm{Tr}\{\mathbf{C}\} = \sum_{u=1}^{U} \lambda_u, \tag{29}$$

where the λ_u are the eigenvalues of $\mathbf{C}$. Therefore, from (28) and (29),

$$\sigma_C^2 = \sum_{u=1}^{U} \lambda_u, \tag{30}$$

which we term the variance of $\mathbf{C}$ and use to appraise field control on the transmission side.

The reflection matrix is defined by $\mathbf{R} = [H_r/H_{iv}]$, where H_r is the reflected field on the input side at $\lambda_0/8$ from the nanostructure, and the corresponding σ_C^2 can be likewise obtained. A large variance indicates that the binary arrangement has a large impact on the scattered field, thus suggesting more control efficacy or increased degrees of freedom for field control.

The force expression we utilize here, originally from Einstein and Laub [53], has been investigated by others [36, 51, 52, 57, 58, 63, 93, 113], and is given by (4) with time convention $\exp(-i\omega t)$ within an isotropic material. We apply a frequency domain finite element method (FEM) to obtain the numerical field solutions [60]. The numerical field solution provides the scattered field, and the total field is obtained by adding the known incident field. The force densities are found using (4), and the pressure obtained from the normalized integral of the force density.

6.5 Pressure in Relation to Field Covariance with Aperiodic Structures

We first investigate the relationship between the nanostructure and both the field and force control with an example metallic material. Gold (Au) with a dielectric constant of $\epsilon = -11.75 + i1.26$ at 633 nm [61] in a free space background is assumed. Figure 9(a) shows results for $f = 0.2$ and Fig. 9(b) for $f = 0.5$. We use (30) to obtain σ_C^2 by randomly selecting 300 arrangements and then a resampling method [101] to obtain the mean $\langle\sigma_C^2\rangle$ and deviation of σ_C^2. Figure 9 shows the statistical results for $\mathbf{T}$ (blue dashed-dotted line) and $\mathbf{R}$ (blue dotted line), along with the deviations, as a function of P. The strong scatter associated with Au scatterers provides relatively larger reflection than transmission, and thus more control on the incident side, exhibited in the larger σ_C^2 associated with reflection. Increasing f increases σ_C^2 under reflection and reduces the control for transmission. With finer discretization through an increase in P, the field control becomes weaker, indicated by a decreasing σ_C^2 in Figs. 9(a) and (b) for both reflection and transmission. We interpret this as being due to the onset of homogenization.

The corresponding statistical data for total pressure with nanostructured Au is shown in Fig. 9 as the orange solid line, along with the deviations for each P. The triangles indicate the maximum total pressure found through this procedure in the positive $\hat{\mathbf{x}}$ direction, resulting in a pushing force. We should note that these results are not the maximum possible pressures. The asterisks show the minimum (with respect to the $\hat{\mathbf{x}}$ direction) pressures found in each case, and some arrangements result in a negative pressure and hence a pulling force on the nanostructure (that can be quite large).

The maximum radiation pressure on a perfect mirror is given by $2S/c$, where S is the magnitude of the incident Poynting vector and c is the free space velocity, with the implication that this is

the background medium. This result was presented by Maxwell and is widely used [59]. With the assumed $S = 1$ W/m^2, the pressure on a perfect mirror is approximately 6.67×10^{-9} N/m^2 with normal incidence. As a reference, this perfect mirror result is plotted as the orange dashed line in Figs. 9(a) and (b), with the understanding that there is no relationship to P. From Fig. 9(a) and for $f = 0.2$, our simulations yielded a maximum positive pressure that is around 5 times larger than that on a perfect mirror. With $f = 0.5$ and from Fig. 9(b), the pressure enhancement can be even larger and reaches around an order of magnitude higher than that on a perfect mirror. Note also that the mean pressure for $f = 0.5$ is higher than the result for the perfect mirror. Worthy of additional comment is the unexpected result that the range of the variances of the total pressure (deviation bars for the orange lines) and the minimum pressure (asterisks) in Figs. 9(a) and (b) indicate that some material arrangements support the total pressures in the negative $\hat{\mathbf{x}}$ direction, namely, pulling against the direction of the incident wave. Gain [93, 114] and control over a particle with a special beam profile [115–117] have been found to produce negative forces, but our results indicate that a structured material with a single incident plane wave can have a net negative force. This pulling force should be important in applications such as optical switching.

We observe from Fig. 9 that a large $\langle \sigma_C^2 \rangle$ for $\mathbf{R}$, the blue dotted line, promotes control of the pushing force, namely the deviation of the positive pressure, and that large $\langle \sigma_C^2 \rangle$ for $\mathbf{T}$, the blue dashed-dotted line, suggests control of the pulling force. As $\langle \sigma_C^2 \rangle$ reduces with increasing P in Fig. 9(a), the deviation and the maximum and minimum pressure also tends to reduce. This is the case for both pushing and pulling, and the relatively high σ_C^2 for $\mathbf{T}$ in this case is indicative of a capacity to enable pulling. The oscillations in the maximum and minimum pressures in Fig. 9(a) relate to resonances, and we will revisit this issue. While the smallest discretization level appears as an anomaly to this trend, we attribute this to insufficient statistics for that case. The relationship between σ_C^2 and pressure is further reinforced in Fig. 9(b), for $f = 0.5$. This large fill case results in small transmission and little field control on that side. The minimum pressures in this case are around zero, showing little control to produce a pulling force. However, σ_C^2 for $\mathbf{R}$ is high in Fig. 9(b), and the pressure deviations and maxima are large. As with $f = 0.2$, a decreasing $\langle \sigma_C^2 \rangle$ corresponds to a reduction in the pressure deviation and the maxima. We conclude that the ability to control fields on the transmission side promotes a pulling force. With an incident H_z, plasmon surface waves are excited. Exciting such surface waves on the back of the aperiodic structure, on the transmission side, can lead to a pulling force. While σ_C^2 measures field control and pressure has the influence of the material properties, with a fixed fill, field control implies force control.

Now we consider aperiodic nanostructured dielectric materials. We choose silicon (Si) as the scattering material because it is important for integrated photonics and has been widely used in nano-scale fabrication. The dielectric constant assumed for Si at a wavelength of 633 nm is $15.07 + i0.15$ [118]. Figure 10(a) shows the near-field field variance (σ_C^2) and pressure data as a function of P, with $f = 0.2$, obtained on a line $\lambda_0/8$ in front of and behind the region discretized, and Fig. 10(b) presents our results for $f = 0.5$. The deviations of the total optical pressure show that the enhancement is overall larger with $f = 0.5$ than that with $f = 0.2$, because the binary nanostructure occupies a larger scattering volume. Similar to the cases for Au scatterers, both σ_C^2 and pressure deviation decrease with increasing P due to homogenization for $f = 0.2$ in Fig. 10(a). We do not observe this trend for $f = 0.5$ in Fig. 10(b), possibly because the large fill fraction has a more stringent (larger) volume requirement to reach homogenization, and the fact that Si offers prospects for high transmission and reflection at high fill. For the Si case, the deviation of the pressures is smaller than those found for Au because of the weaker scatter. However, the maximum radiation pressure can still reach around 3 times larger than that on a perfect mirror, shown again as the orange dashed lines in Fig. 10. Figures 10(a) and (b) show that Si aperiodic structures can also provide a pulling force. Both fills offer substantial negative pressures, as indicated by the asterisks. We understand this by the relatively high transmission compared to the equivalent cases

for Au. The deviation and the maximum values of the pressure are larger for the higher fill case. Our results show that dielectric materials are also good candidates for optical pressure enhancement and optomechanical applications. Both pushing and pulling pressures can be substantial greater than that on a perfect mirror.

The σ_C^2 data in Fig. 10 for Si again provides insight into the pressure. When $f = 1$, $\sigma_C^2 = 0$, so the increasing fill will eventually result in loss of field control and hence, presumably, reduced pressure enhancement. Resonant features can be observed in the results for $\langle\sigma_C^2\rangle$ as a function of P, as found in earlier work [101]. The cases in Fig. 10(a) where the local maximum $\langle\sigma_C^2\rangle$ from the transmission matrix $\mathbf{T}$ (for example, the blue dashed-dotted line for $P = 7$) and the local maximum $\langle\sigma_C^2\rangle$ from the reflection matrix $\mathbf{R}$ (for example, the blue dotted line with $P = 5$) are suggestive of series-resonance (high transmission) and parallel-resonance (high reflection), respectively. Corresponding to these observations for $\langle\sigma_C^2\rangle$, the mean pressure for $P = 5$ is larger than for $P = 7$. Consequently, given the pressure deviations for these two levels of discretization, the parallel resonance ($P = 5$) is likely to result in pushing, but the statistical data for pulling with series resonance ($P = 7$) is inconclusive for this fill. The case for $P = 5$ in Fig. 10(b) has large $\langle\sigma_C^2\rangle$ for $\mathbf{R}$ and a correspondingly large mean pressure, whereas for $P = 7$, where $\langle\sigma_C^2\rangle$ dips, there is a small mean pressure. This again suggests control of the reflected fields promotes pushing. Consider now $P = 11$, which has the largest $\langle\sigma_C^2\rangle$ for $\mathbf{T}$ and also large $\langle\sigma_C^2\rangle$ for $\mathbf{R}$, possibly supporting both series and parallel resonances and providing the largest pressure deviation and promoting substantial pulling. Our conclusion is that for both dielectric and metallic scatterers, σ_C^2 is a useful metric to investigate pressure.

6.6 The Influence of Field Resonances on Pushing and Pulling

The statistical results from Figs. 9 and 10 show oscillatory features as P is varied. These variations are prominent in the $\langle\sigma_C^2\rangle$ data in Fig. 10, but also clearly evident in the maxima and minima of the pressures for both the Au and Si structures. This data suggests field resonances within the structures and, importantly, that these may play a role in achieving large positive or negative pressure. Here, we investigate the physical resonance effects within the binary materials by observing the field and corresponding optical force density distribution for specific material instances with maximum pushing/pulling optical force.

Consider the case for Au in Fig. 9(a) for $f = 0.2$ with the maximum pushing force, which occurs when $P = 6$ ($\{P, P\} = \{6, 6\}$, where the triangle indicates a pressure of about 3×10^{-8} N/m^2). Figure 11(a) shows the binary nanostructure arrangement for this case. The magnitude of the electric and magnetic field distributions with normal incidence is given in Figs. 11(b) and (c), respectively. Figure 11(d) shows the time-averaged optical force density, $\langle \mathrm{f_x} \rangle = \langle \mathbf{f} \cdot \hat{\mathbf{x}} \rangle$, from (4). The magnitude of the electric field and the force density distributions are normalized to 1 V/m and 1 N/m^3, respectively, and presented on a log scale (dB) in order to distinguish the large contrast in the local values. The relatively large reflected fields can be observed in both Figs. 11(b) and (c), and there is evidence of plasmon surface waves that have a substantial influence on the force density in Fig. 11(d). Notice that significant reflection and control over the reflected fields, as measured by σ_C^2 in Fig. 9(a), promotes a large pushing force. In an equivalent circuit sense, this corresponds to a parallel resonance, thereby inducing a large reflection.

Next, we consider the case of Au with the same resolution, $P = 6$, but supporting the maximum pulling force (the asterisk in Fig. 9(a)). The arrangement of Au scatterers for this example is shown in Fig. 12(a). We plot the magnitude of the electric and magnetic field distributions in Figs. 12(b) and (c), respectively. Figure 12(d) shows the force density $\langle \mathrm{f_x} \rangle$. A larger proportion of negative (in the $-\hat{\mathbf{x}}$ direction, namely, pulling) force density can be found within each scattering element, and this results in the cumulative negative pressure. Different from the field distributions in Fig. 11 for the pushing case, the larger fields on the transmission side can be observed in Figs. 12(b) and (c), consistent with a series resonance. Note the surface wave excited on the right-hand side of the

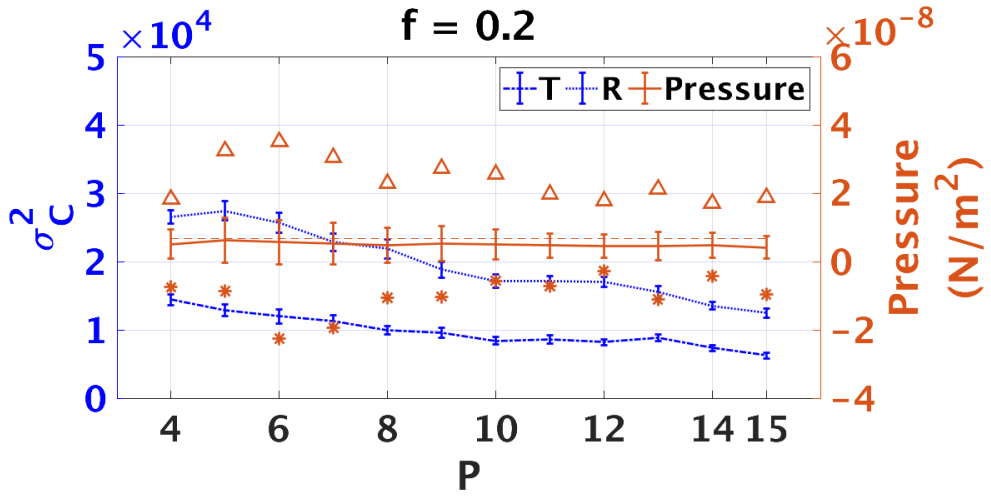

(a)

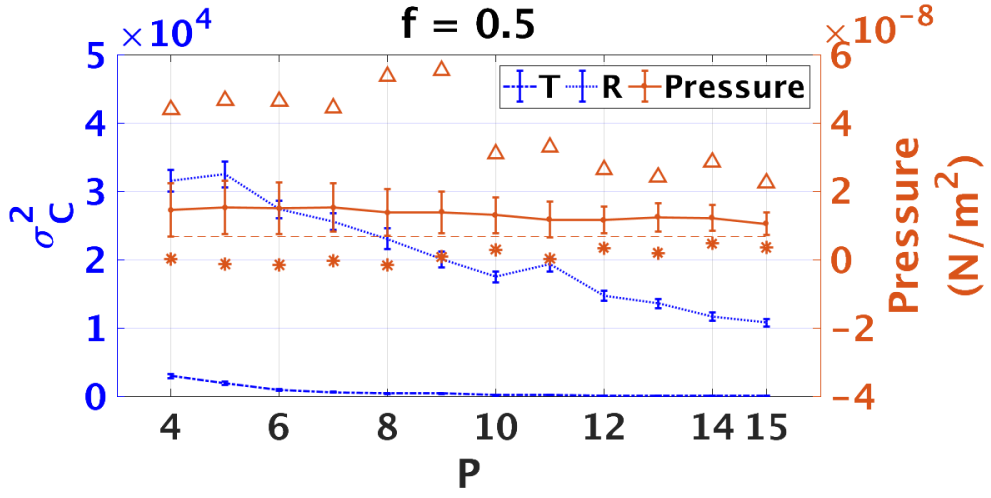

(b)

Figure 9. The variance for aperiodic nanostructured Au, σ_C^2, measured $\lambda_0/8$ from the discretized domain, and the optical pressure as a function of discretization, P, with fill fraction: (a) $f = 0.2$ and (b) $f = 0.5$. Referring to Fig. 8, the magnitude of the normally incident power density is 1 W/m^2. The blue dotted line and blue dashed-dotted line, relate to the left axis and describe σ_C^2 from the reflection and transmission matrices, $\mathbf{R}$ and $\mathbf{T}$, respectively. The standard deviation bars were calculated from a resampling method. The orange solid line refers to the right axis and describes the corresponding radiation pressure on the binary material and the deviations from the analysis. The orange dashed line indicates the maximum pressure on a perfect mirror. The triangles and asterisks show the maximum and minimum radiation pressure, respectively, in the direction of the incident wave ($\hat{\mathbf{x}}$ direction). The pushing and pulling forces correlate with σ_C^2 from the reflection and transmission matrices $\mathbf{R}$ and $\mathbf{T}$, respectively.

structure that is very evident in the magnetic field plot of Fig. 12(c). Excitation of a surface wave on the back can lead to a pulling force.

The fields in Fig. 11 for a pushing case and Fig. 12 for a pulling situation are consistent with the statistical results we found for σ_C^2 in Fig 9(a). A large σ_C^2 for reflection, as for $f = 0.2$ in Fig. 9(a), implies a larger maximum pushing force. Conversely, the large σ_C^2 for transmission for $f = 0.2$ in Fig. 9(a) results in a larger pulling force. This reveals that the fields excited by the arrangement in front of or behind the binary nanostructure relates to whether the whole geometry is pushed or pulled and to the pressure enhancement.

We observe that the arrangement of binary elements within the nanostructure plays an important role on determining the direction and enhancement of the optical force. In Fig. 11, when the

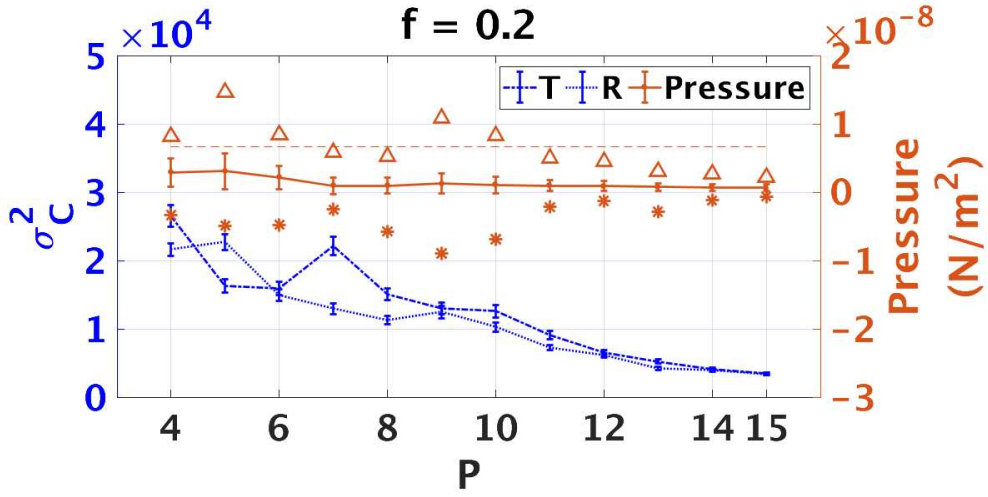

(a)

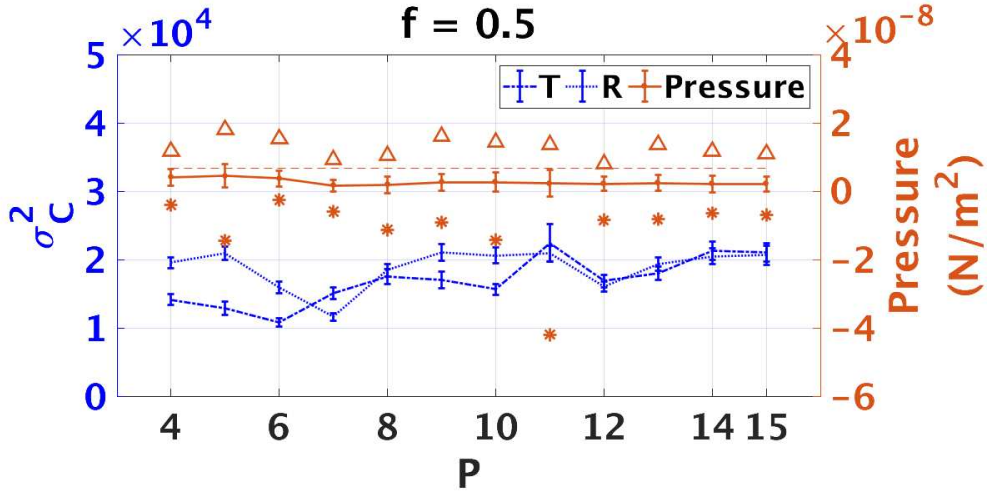

(b)

Figure 10. The variance for aperiodic nanostructured Si, σ_C^2, measured $\lambda_0/8$ from the discretized domain, and the optical pressure as a function of discretization, P, with fill fraction: (a) $f = 0.2$ and (b) $f = 0.5$. The magnitude of the normally incident power density is 1 W/m^2. The blue dotted line and blue dashed-dotted line, refer to the left axis, describe σ_C^2 from $\mathbf{R}$ and $\mathbf{T}$, respectively. The standard deviation bars were calculated from the statistical analysis. The orange solid line refers to the right axis and describes the corresponding radiation pressure on the binary material, and the bars show the standard deviations in the samples. The orange dashed line indicates the maximum pressure on a perfect mirror. The triangles and asterisks show the maximum and minimum radiation pressure, respectively, in the $\hat{\mathbf{x}}$ direction. Aperiodic dielectric structures can also support both enhancement and the control of the direction of the optical force.

scattering elements pack together to form a strip, the arrangement is effectively a slab of a particular length. The resulting surfaces can produce plasmon mode resonances. Those transverse resonances are most pronounced in Fig. 11(c), adjacent to the PEC walls at the top and bottom, and the surface wavelength in relation to the element size can be understood with use of symmetry from the boundary (the PEC is an even boundary for H_z). In the metallic case, certain arrangements can lead to very large surface fields, and hence to substantial enhancement in the pressure.

Figures 13 and 14 show the fields and force densities for maximum pushing and pulling situations with Si scatterers. Figure 13 is for $f = 0.5$ and $P = 5$ and the largest pushing force, where there is a σ_C^2 peak for reflection in Fig. 10(b). Note again the substantial amplitude of the reflected fields. However, while the metal cases supported surface waves, here the fields are confined within the

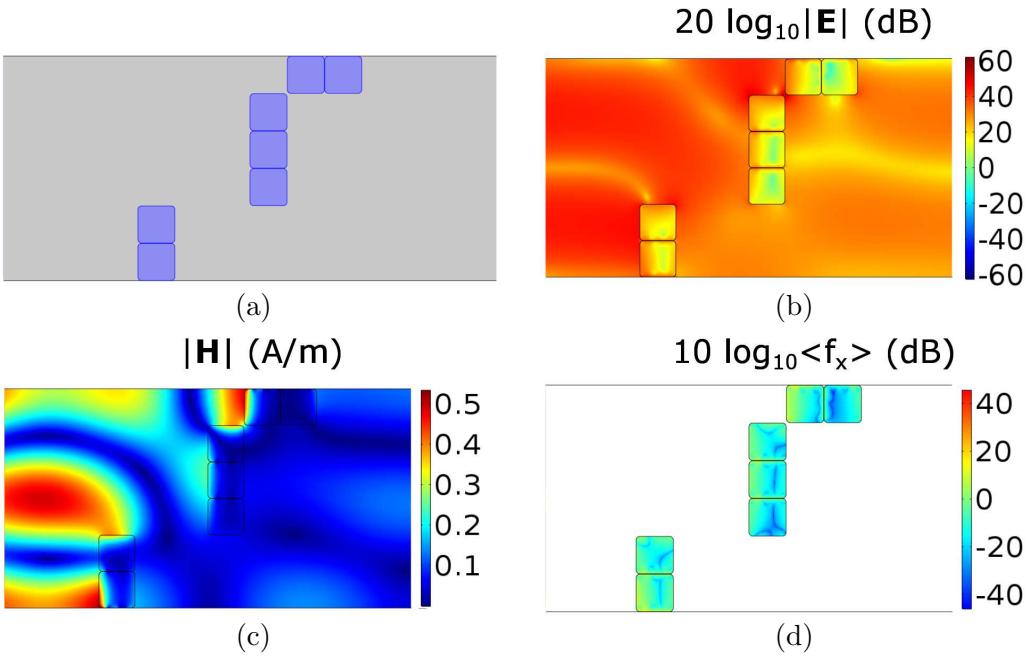

Figure 11. The fields and force density for the arrangement in Fig. 9(a) for Au with the largest pushing force: $\{P, P\} = \{6, 6\}$ and $f = 0.2$. (a) The purple squares indicate the positions of the scatterers. (b) The electric field magnitude, normalized to 1 V/m on a log scale (dB). (c) The magnetic field distribution. (d) The time-averaged optical force density, $\langle \mathrm{f_x} \rangle = \langle \mathbf{f} \cdot \hat{\mathbf{x}} \rangle$, normalized to 1 N/m^3 on a log scale (dB). The parallel-resonant condition in this example supports the enhanced pushing pressure.

dielectric. The element size in Fig. 13(a) is more than $\lambda_0/(2\sqrt{\epsilon})$ and hence can support a resonant mode. Local resonances are evident in the magnetic field magnitude in Fig. 13(c). Figure 14 is for $f = 0.5$ and $P = 11$, the largest pulling force case in Fig. 10(b). Note the large field resonances that span two or more adjacent scatterers, and the large transmitted field. As with the Au scatterer case, there is a consistent picture of large σ_C^2 for the reflected field implying a large pushing force and large σ_C^2 for transmission indicating opportunities for pulling.

Conservation of energy requires that the power flow on the transmission side should be less than that on the incident side. We calculated the power densities for reflected and transmitted fields in the $\hat{\mathbf{x}}$ direction (see Fig. 8) on the incident and transmission sides, respectively, $\lambda/2$ away from the aperiodic structure, and then integrated along the $\hat{\mathbf{y}}$ direction and divided by the length (633 nm) to obtain the averaged reflected (S_r) and transmitted (S_t) power densities. Those results, as reflected and transmitted power flow (W/m^2) with incident $S_i = 1$ W/m^2, are: 0.228, 0.187 (Fig. 11); 0.469, 0.167 (Fig. 12), 0.274, 0.325 (Fig. 13), and 0.212, 0.102 (Fig. 14). It is clear that S_t is less than $S_i - S_r$ in all cases, and that the energy is conserved in the simulations we considered.

6.7 Discussion and Applications

Our approach of investigating the statistical fields and pressures in binary aperiodic metal and dielectric structures sought to uncover the relationship between structure and force for basic understanding and to guide a design process in applications. We used σ_C^2 to measure field control and related this to pressure control. Because of the 2D analysis, it was clear that magnetic field should be used in this statistical field analysis. However, we should note that the electric field information that is relevant in the force density of (4) is then indirectly measured.

The statistical pressure study we presented provides a way to explore the parameter space for a binary structure class with a large number of variables. Consequently, one can determine possible pressure enhancement opportunities and also obtain a guide for the design process with constraints. For example, we have learned that with a given fill fraction, Au provides a larger pushing force

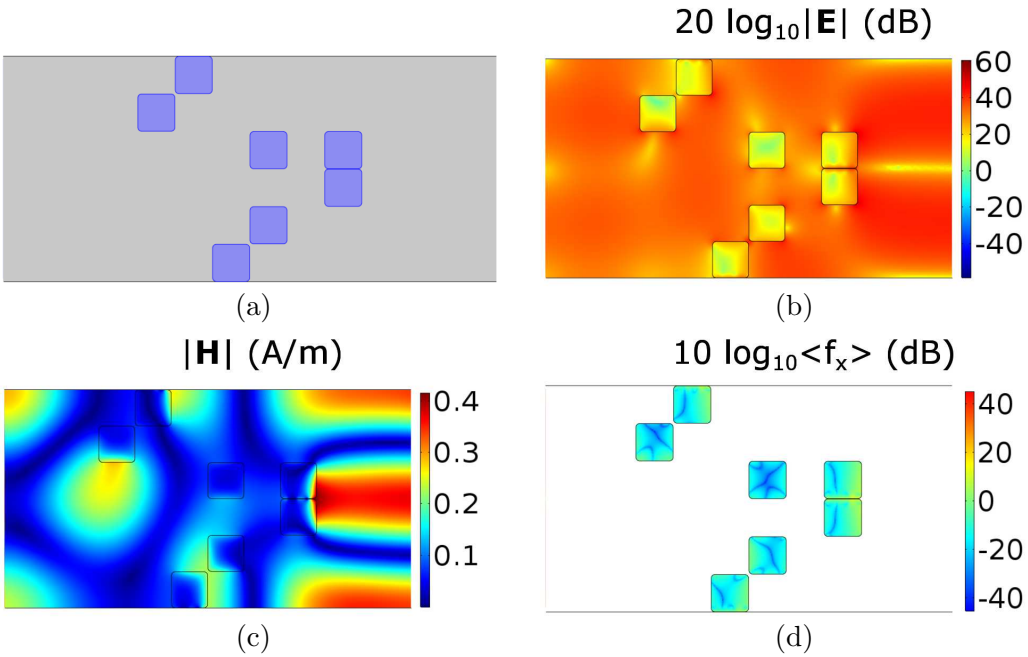

Figure 12. The fields and force density for the arrangement in Fig. 9(a) for Au with the largest pulling force: $\{P, P\} = \{6, 6\}$ and $f = 0.2$. (a) The purple squares indicate the positions of the scatterers. (b) The electric field magnitude, normalized to 1 V/m on a log scale (dB). (c) The magnetic field distribution. (d) The time-averaged optical force density, $\langle f_x \rangle$, normalized to 1 N/m^3 on a log scale (dB). A pulling force on the scattering material is induced when the series-resonant condition occurs.

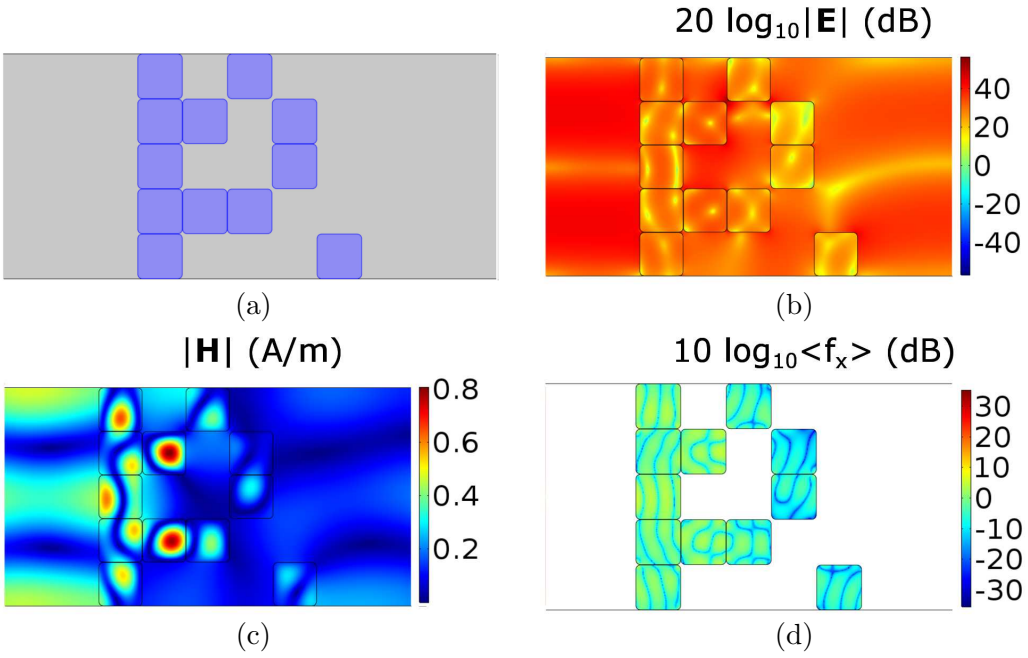

Figure 13. (a) Referring to Fig. 10(b) for Si, the aperiodic binary nanostructure with $\{P, P\} = \{5, 5\}$, $f = 0.5$ that produced the maximum pushing force from the samples studied. The purple squares indicate the positions of the scatterers. (b) The electric field distribution, normalized to 1 V/m on a log scale (dB). (c) The magnetic field distribution. (d) The time-averaged optical force density $\langle f_x \rangle$, normalized to 1 N/m^3 on a log scale (dB). The Si pillars that form cavities in this example support the pushing pressure enhancement.

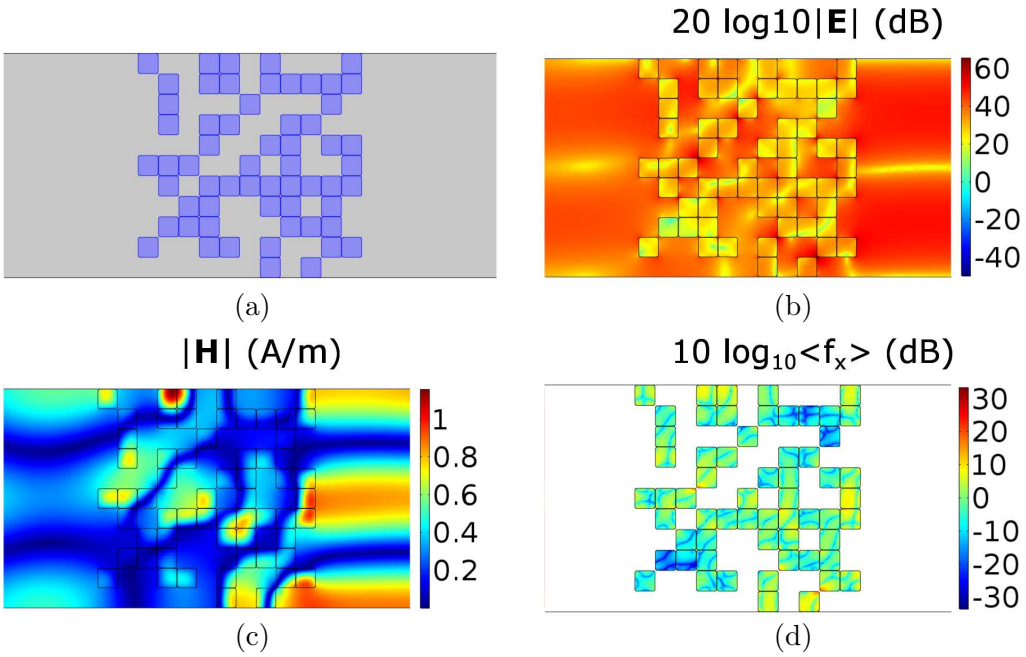

Figure 14. (a) Referring to Fig. 10(b) for Si, the aperiodic binary nanostructure with $\{P, P\} = \{11, 11\}$, $f = 0.5$ giving the maximum pulling force in the samples over the scatterers. The purple squares indicate the positions of the scatterers; (b) The electric field distribution, normalized to 1 V/m on a log scale (dB). (c) The magnetic field distribution. (d) The time-averaged optical force density $\langle \mathrm{f_x} \rangle$, normalized to 1 N/m^3 on a log scale (dB). The pulling force on the scattering materials is induced when the fields percolate through the Si scatterers and allow excitation on the back.

enhancement than Si. Also, a lower fill fraction promotes pulling for Au, but for Si, the high fill facilitated pulling.

The use of σ_C^2 for the reflected or transmitted fields provides a relevant measure. However, this may not be available in a design situation. Our formation of a link between fields and field correlations and the force density and pressure is intended to provide fundamental insight. This could be used in a discrete optimization design approach [110] to reduce the computational burden. For instance, this might guide the material choice, discretization level, and spatial support. Beyond binary materials, mixture theory provides a way to tune the dielectric constants, and the boundaries could be adjusted, both as part of a continuous optimization process [106, 108]. The binary picture is then a coarse discretization in both space and material.

The fact that an incident plane wave can produce a pulling force may be unexpected, given earlier work where a pulling force on a bead was achieved with structure in the incident field [115, 116]. As we have explained in relation to Figs. 12 and 14, pulling occurred with large transmission through the structure. This was facilitated by Au with small fill or use of Si. Establishing fields on the back of the structure appears to facilitate pulling. We suggested this was established along the lines of a series resonance, in the equivalent circuit sense. However, more generally, we understand this effect as one of modifying the scattered field in a way that when superimposed with the incident field, the total field produces a force density such that pulling occurs. We should also note that this pulling force can be substantially larger than $2S/c$, based on the results we presented. A negative pressure should be important in remote control applications because a surface could be both pushed and pulled. While we have not established that this is possible in a given material, we anticipate that this could be achieved by using two different wavelengths for the incident light and designing the structure accordingly to support spectrally controlled motion.

The high transmission when there are effectively cascaded elements, as in Fig. 12 for Au, implies that optical percolation has occurred. A large total field therefore accumulates on the right side of

the binary material system, potentially resulting in a pulling optical force (opposite to the direction of the incident light). There is therefore in principle a link between pressure and percolation theory [119, 120].

Various applications may benefit from the study we have presented. Biomolecules have been attached to beads to impart a force using optical tweezers, and this provides useful biophysical information [102]. By structuring the bead, a larger force could be imparted, and this would mean a reduction in the required laser power. It may also be useful to have a large, structured material that provides a pushing or a pulling force in such experiments. Light sails have been used with solar propulsion. However, with structured material, a laser of the appropriate wavelength could be used. It may also be useful to use incoherent solar radiation for propulsion with aperiodic structured material, but the tradeoff between wavelength diversity and the exploitation of resonance effects to enhance the force needs to be investigated. The propulsion force (magnitude and direction) could in principle be regulated, allowing control over the trajectory of the vehicle. The deflection of an optical beam is important in displays and communication. With both pushing and pulling, a more versatile control element would be possible. It should also be expected that the principle of structured material for the control of optical forces will translate to integrated photonics. All-optical communication, rather than electronic control of photonic networks, has the promise of a substantial reduction in energy consumption [121, 122]. The use of dielectric nanostructured materials should benefit optical communication in Si-based technology. In this approach, the force imparted due to light would lead to switching, and pushing/pulling manipulation could be utilized. Our results motivate the further development of fabrication technology for aperiodic structures in optomechanical applications. Earlier work has presented ways to fabricate aperiodic waveguides [108], and an on-chip platform for controlling light-matter interactions in turbid media [123]. For example, direct nanoimprinting into metal can be used to realize nanophotonic elements [100], and that method could be used to fabricate surface-based aperiodic elements, possibly in a planarized layered arrangement.

7 Demonstration of Enhanced Optical Pressure on a Structured Surface

7.1 Summary

The interaction of electromagnetic waves with condensed matter and the resultant force is fundamental in the physical sciences. The maximum pressure on a planar surface is understood to be twice the incident wave power density normalized by the background velocity. We demonstrate for the first time that this pressure can be exceeded by a substantial factor by structuring a surface. Experimental results for direct optomechanical deflection of a nanostructured gold film on a silicon nitride membrane illuminated by a laser beam are shown to significantly exceed those for the planar surface. This enhanced pressure can be understood as being associated with an asymmetric optical cavity array realized in the membrane film. The possible enhancement depends on the material properties and the geometrical parameters of the structured material. Such control and increase of optical pressure with nanostructured material should impact applications across the physical sciences. This work has been published in Physical Review Letters [91].

7.2 Design

The pressure on a mirror can be understood at the atomic level, where there is a momentum exchange between the photon and the atom that can be influenced by the environment [50]. At the macroscopic material level, the optical force on a surface has been described by a pressure given by (6) [59]. Consequently, the maximum pressure from (6) is $P = 2S/c$ N/m^2. However, (6) precludes information on how the field interacts with the material. A fundamental approach is to describe the optical force density in the material in terms of fields using (4). The more general form of (4) has been used to describe key experiments [51, 58], is consistent with a development from Einstein

and Laub [53], and results in the theory of Lorentz in the static limit [63]. Solving for the fields in a planar gold (Au) mirror with plane wave illumination using (4), where the second term is zero with normal illumination, leads to the force density and hence a pressure that is very close to that from (6) with $|\Gamma| = 1$. This pressure on a planar surface thus provides a good reference for the results we present. While (6) provides a reasonable description for the force on a planar surface with no transmission, (4) allows the 3D structured material situation to be treated, where both the cross and gradient terms contribute to the pressure with a structured material.

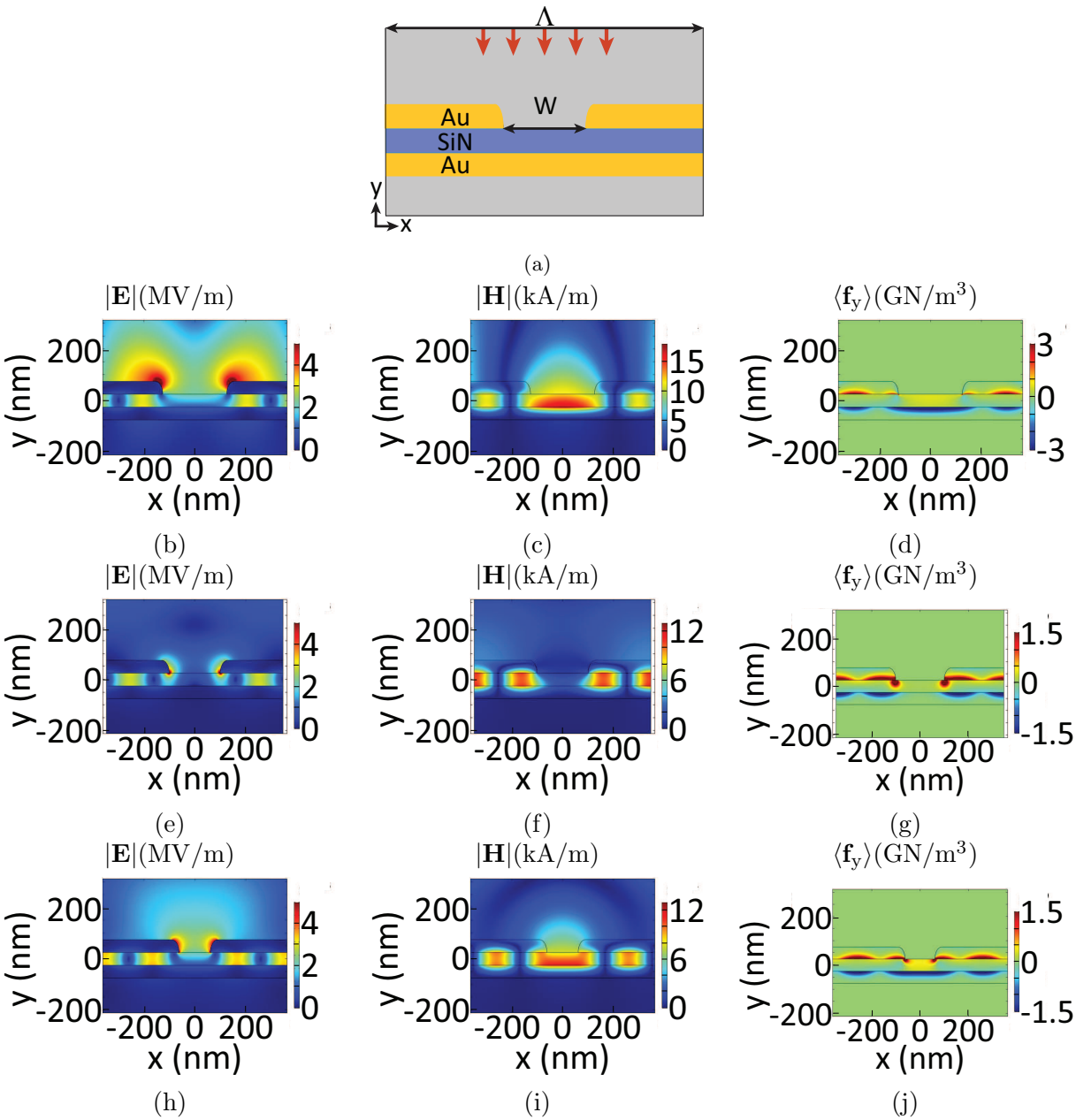

Figure 15. Simulated fields and force densities for the periodic slot structure of Fig. 1(b): (b)-(d) Strong Push, $\Lambda = 966.4$ nm, $W = 250$ nm, $P = 25.7$ N/m^2; (e)-(g) Strong Pull, $\Lambda = 692.2$ nm, $W = 200.4$ nm, $P = -20.2$ N/m^2; (h)-(j) Weak Push, $\Lambda = 886$ nm, $W = 124$ nm, $P = 3.26$ N/m^2. The slot taper was determined according to SEM data from fabricated samples. The power density for the 1070 nm plane wave is 318 MW/m^2, corresponding to 1 mW over a 1 μm radius circle.

Figure 15(a) shows the simulation geometry of the partial-depth taper slots, where the thickness of Au and SiN are both 50 nm, and W and Λ are the slot width and the periodicity, respectively. The simulated field and optical force densities for three geometries that were fabricated are shown in Fig. 15, and W and Λ, and the calculated pressure, P, for each are given in the caption. The plane wave (E_x, H_z) normally incident from the top has a power density of 318 MW/m^2, roughly 1 mW over a 1 μm radius circle. Figures 15(b)-(d) show a strong pushing force (Strong Push) situation (25.7 N/m^2) in the direction of the incident Poynting vector, Figs. 15(e)-(g) a strong pulling force (Strong Pull, -20.2 N/m^2), and Figs. 15(h)-(j) a weak pushing (Weak Push) force (3.26 N/m^2). The corresponding calculated pressure on the planar Au-SiN-Au film is 2.11 N/m^2 and on a perfect mirror is 2.12 N/m^2. The dissipated power density from optical absorption calculated in each case is: 227.9 MW/m^2 (Strong Push), 141.8 MW/m^2 (Strong Pull), and 143.9 MW/m^2 (Weak Push). The planar surface power dissipation is 22.6 MW/m^2. The intent was that the weaker pushing force case to be similar in magnitude to the planar case, and to be substantially smaller than those for the strong pushing and pulling structures. Numerical convergence studies based on element size refinement and slight rounding of the corners ensured the accuracy of the solutions for both the fields and the force densities. There is a metal-insulator-metal (MIM) waveguide mode established involving the Au and SiN interfaces that produces rather symmetric and competing force densities. A resonant surface wave at the Au-SiN interface at the bottom of the slot, clear in Fig. 15(c), provides the major pushing force, as is evident in Fig. 15(d). This phenomenon, with the relatively wide slot width, differs from the vertical MIM cavity array that produces an enhanced pressure [52]. The primary contribution to the pulling force is in the neighborhood of the Au slot, near the SiN surface, as Figs. 15(e) and (g) show for the field and force density, respectively. In this case, the scattered fields have been adjusted (by varying W and Λ) to produce a total field that imparts a net negative force. On the contrary, tractor beams pulling beads operate by control of the incident beam [115], although of course it is the total field also that imparts the force. The weak pushing force described in Fig. 15(j) results from competition between pushing and pulling forces.

We understand enhanced optical pressure, identified as a magnitude greater than $2S/c$, where S is the incident Poynting vector magnitude and c is the speed of light in vacuum, as being based on the excitation of resonances in the material. In the situations treated, the surface plasmon waves resonate. By controlling the geometry variables, the character of the fields and their resonances regulate the force density hence the pressure.

7.3 Fabrication

We fabricated partial-depth slots using the designs of Fig. 15. While structures like Fig. 3 could be fabricated using a nanoimprint method we have presented [124], it is easy to build slots with FIB milling. Because of our interest in characterizing a variety of structures, we decided to initially focus on this fabrication method, and to incorporate milling tapers into the designs.

We developed FIB milling during our earlier work [125–129]. The resolution depends on the ion current used (smallest current available), the ion stability, and the metal material on which the patterns are to be written. Another factor affecting the resolution is the thickness of the metal film. Due to the tapered profile of the focused ion beam, one will obtain a wider opening on one side of the surface and a sharp opening on the other side, while milling a structure such as a slot. The partially cut-through slots can be achieved by controlling the current and milling time.

We started with commercially available SiN membranes having a thickness of 50 nm (Norcada, Inc.). These membranes had dimensions of 500μm $\times$ 500μm and were supported on a frame made of silicon. Gold was deposited on both sides of the membrane using an e-beam evaporator (CHA), following deposition of a 5 nm layer of titanium for adhesion. Thus, essentially a three-layered symmetric structure made of Au-SiN-Au was formed bounded on all sides by the Si support structure, as shown in Fig. 16(a). This sample was used to study the deflection response of a planar surface under the influence of an incident pressure laser.

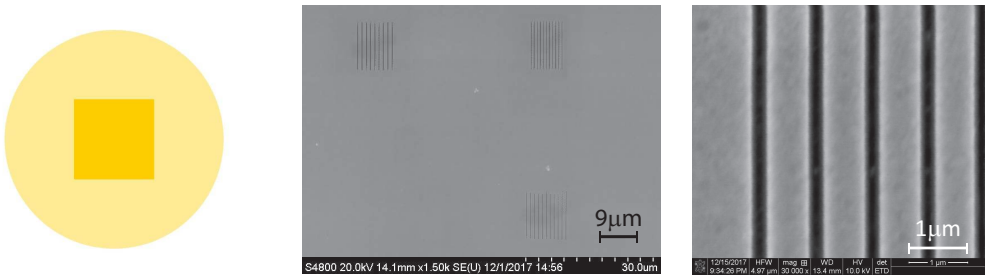

(a) (b) (c)

Figure 16. (a) Schematic of the top view of the three layered Au-SiN-Au membrane, and SEM images of: (b) The three slot arrays with an enhanced pushing force (Strong Push, top left), an enhanced pulling force (Strong Pull, top right), and a weak pushing force (Weak Push, bottom right). SEM image data indicates: all slots have a length of 11.5μm; for the Strong Push structure, 9 slots with $W = 250 \pm 2.2$ nm, $\Lambda = 966.4 \pm 7.7$ nm; for the Strong Pull structure, 11 slots with $W = 200.4 \pm 3.4$ nm, $\Lambda = 692.2 \pm 7.3$ nm; and for the Weak Push structure, 11 slots with $W = 124 \pm 3.3$ nm, $\Lambda = 886 \pm 9.8$ nm. (c) A higher magnification SEM of the Strong Push slot array.

Next, three periodic slot array structures were milled near the center of the membrane with nominal dimensions corresponding to those used in the simulations in Fig. 15 and measured dimensions indicated in the caption of Fig. 16. The SEM (Hitachi S-4800) image for these slot arrays is shown in Fig. 16(b). A fourth symmetric location was used for the planar deflection data. A magnified image of the large pushing force structure (top left of Fig. 16(b)) is shown in Fig. 16(c). Images from an SEM with an edge detection method that defines the edges from the local maximum gradient of the image intensity [130] provided precise geometry information for the fabricated structures for analysis and extraction purposes.

7.4 Experimental Results

We measured the membrane deflection under the influence of the force from an illuminating laser beam. Figure 17(a) shows how a quadrant (quad) photodetector with a low-power, 640 nm sensing laser was utilized for measuring the deflection of the membrane. The membrane was mounted on a holder whose position could be controlled with a motorized stage. The detection laser was incident on the position exactly opposite the pressure laser and on the top, planar side of the Au-coated membrane. The schematic for the experiment is shown in Fig. 17(b). The 1070 nm pressure laser deflects the membrane, thus changing the position of the sensing laser on the four quadrant photodiode. The photodiode provides a voltage reading which is then converted into the actual deflection by calibrating the change in voltage with a known change in displacement.

Referring to Fig. 17(b), the 1070 nm CW fiber laser (S1) passes through a chopper and illuminates the membrane. A neutral density filter (ND) and a polarizer (P) control the incident power on the sample and polarization. TM (magnetic field out of the page in Fig. 17(a)) polarization is used in the experiments which gives an enhanced optical force with the slots. An objective lens (O) is placed near the sample to focus the force laser beam on the desired position of the sample. The input laser beam is intensity modulated at a particular frequency with the help of a chopper (C) that is synchronized with a lock-in amplifier (LA) to reduce the measurement noise. We used CCD camera to observe the reflection image of the sample with illumination of white light (WL) to determine the position of the focused spot from the force laser. The deflection of the sample is measured on the other side of the sample with the help of a detection laser, a 640 nm CW laser (S2). The detection laser monitors the deflection of the membrane through the quadrant photodiode (Quad) and can be recorded on the oscilloscope (OC) and the lock-in amplifier (LA).

We illuminated the membrane with the pressure laser and scanned the membrane to obtain deflection as a function of incident laser position on the membrane. This allowed location of the center of the slot arrays from the locations for local maximum deflection. Figure 18 shows the scanning results of the membrane region including the three slots and the corresponding symmetric planar

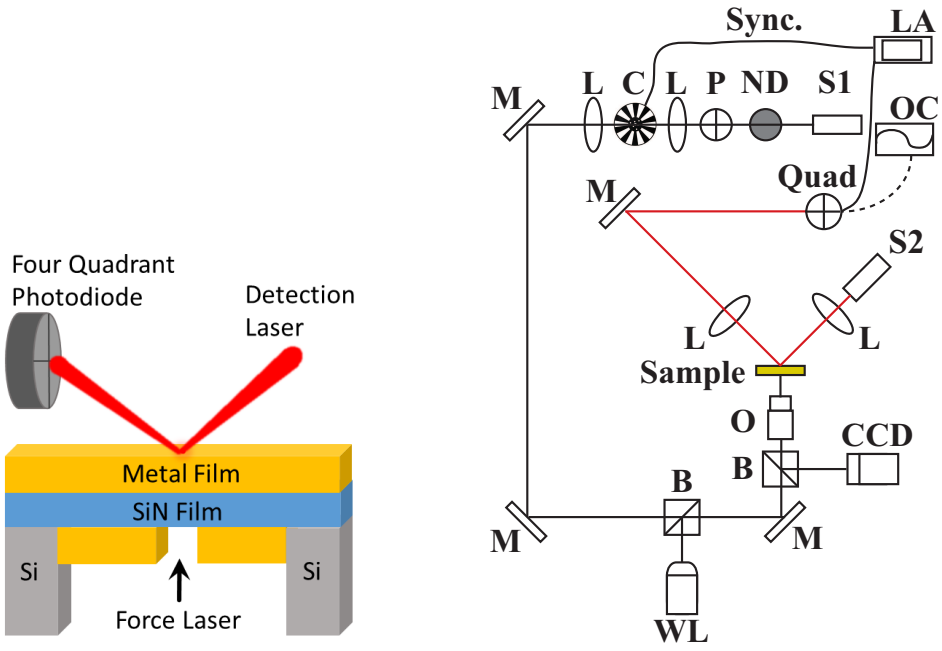

(a) (b)

Figure 17. (a) The quadrant detection system for monitoring deflection that uses a 640 nm diode laser. (b) The deflection experiment. S1: Force laser (operates at 1070 nm); S2: Detection laser (640 nm); Quad: Quadrant photodiode; OC: Oscilloscope; LA: Lock-in amplifier; ND: Neutral density filter; WL: White light source; P: Polarizer; C: Chopper; O: Objective lens; M: Silver mirror; B: Beam splitter; L: Lens.

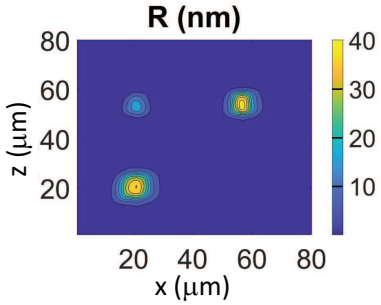

Figure 18. Scanned membrane deflection magnitude measured using a lock-in amplifier as a function of position in the region containing the three slot arrays, with 1 mW incident power at 1070 nm.

surface location with 1 mW incident power. The deflection signal is from the lock-in amplifier, and the magnitude in Fig. 18 indicates displacement. The phase information can be used to determined the direction of total deflection, and this was verified by oscilloscope data. The direction of the total deflection of the three slotted areas and the planar surface area are all towards the sensing laser side.

The measured (total) deflection is shown in Fig. 19(a) by the solid circle points and the dotted lines are a least mean square error fit for optical powers less than 1 mW, selected so that all of the data is in the small signal, linear regime (with respect to force laser power). The dotted lines are treated as the measured data for the three slot arrays and the planar surface. All four measurement locations on the membrane have the same deflection direction, towards the sensing laser side (and in the direction of the incident force laser). The total deflection in Fig. 19(a) for the Strong Push case is largest, followed by the Weak Push, Strong Pull, and, far smaller, the Planar case. The Strong Pull total deflection is less than the Weak Push because the optical force is in the opposite direction to the thermally-driven deflection. The measurement error bars (that are more pronounced in the

expanded view) were determined based on 100 measurements with the lock-in amplifier (10 ms integration time for each datum and a total duration of 1 s), and are found to be negligible for our purposes.

The total deflection has contributions from both the direct optical force and heating. When the 1070 nm laser illuminates the Au-coated membrane, heat will be generated that will result in thermal-based deflection. We have devised a mean to separate the direct optical deflection from the thermal deflection. For a given membrane, the mechanical properties should be fixed, and we assume that they are independent of position over the measurement domain. Also, in the small deflection regime, there is a linear relationship between optical power and deflection, and between displacement and force (given by the spring constant) and heating. Consequently, the superposition of the direct optical deflection and the thermally-driven membrane deflection holds. From simulations, we generate the optical force from (2) and the dissipated power (due to the imaginary parts of the material parameters) for each structure and the planar membrane. These will of course vary with the geometry (for example, for different slot structures). However, assuming the model is correct, it is possible to use a fitting parameters that relate the calculated optical force to deflection (α m/N) and the thermal dissipation to deflection (β m/W). These parameters can be obtained using adequate experimental data. The validity of this approach is then measured by the ability to predict independent measurements, or equivalently, the quality of the fit between the predicted and measured deflection results. In this manner, the legitimacy of the force model can also be appraised. The deflection for each measurement (either position of the optical beam on the membrane or the power level at a fixed position) can be written as

$$\begin{aligned} \alpha F_1 + \beta T_1 &= D_{\mathrm{t}1} \\ \alpha F_2 + \beta T_2 &= D_{\mathrm{t}2} \\ &\vdots \quad , \\ \alpha F_{\mathrm{K}} + \beta T_{\mathrm{K}} &= D_{\mathrm{t}\mathrm{K}} \end{aligned} \tag{31}$$

where F_k, $k = 1, 2, ..., \mathrm{K}$ is the calculated optical pressure from the simulation, T_k is the calculated power dissipation from the simulation, and $D_{\mathrm{t}k}$ is the measured total deflection. The first term on the left hand side represents the optical deflection while the second term describes the thermal deflection. We determine α and β using least squares fitting. Four sets of F_k and T_k, the enhanced pushing force, the enhanced pulling force, the weak pushing force, and the planar surface, were used in the fitting process (so $\mathrm{K} = 4$). As a result, the optical deflection can be extracted from the total deflection.

We use the dotted line fits in Fig. 19(a) to form dD_{tk}/dP_o, with P_o the variable force laser power, and then a least squares fit to estimate a single α and β for dF_k/dP_o and dT_k/dP_o, respectively, that hold for all structures. The accuracy of this procedure is clear in predicting all experimental data, as shown in the deflection results of Fig. 19(a).

Figure 19(a) shows the results with two modeling approaches: a simple 2D periodic structure assumed for each slot array with plane wave illumination (solid), and a more accurate 3D Gaussian beam illumination of each slot array with a sequence of 2D slice solutions accounting for the beam profile along the length of the slots (dashed). The fields and force densities for each finite-width structure with a Gaussian incident field ($1/e$ field at a half-width of 7μm) was found to have similar key features to the 2D periodic case with plane wave illumination. The 2D slice approximation of the 3D solution was investigated by calculating the 3D force and dissipation on a planar (Au-SiN-Au) surface by comparing with results from a superposition of 2D slices, and found to be satisfactory. The simulated results use the experimentally-derived α and β to relate calculated force and dissipation, respectively, to displacement. The simulated total deflection results using the periodic assumption (with the mean width and period of each array) compare favorably with

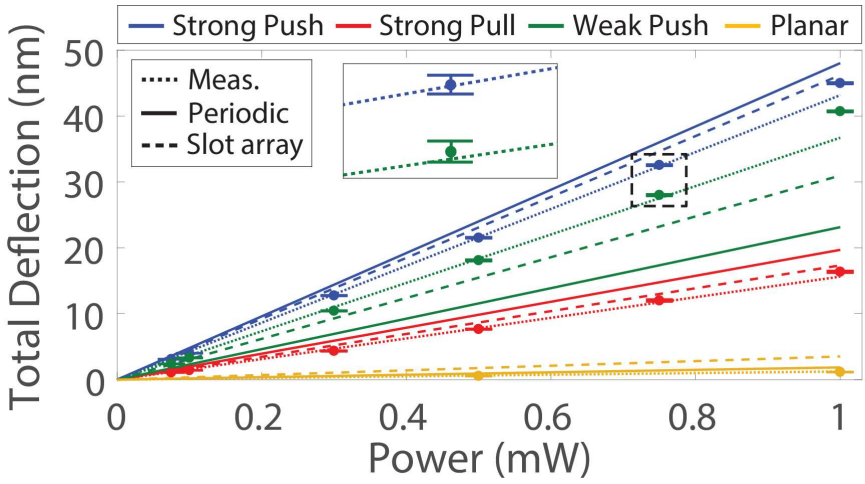

(a)

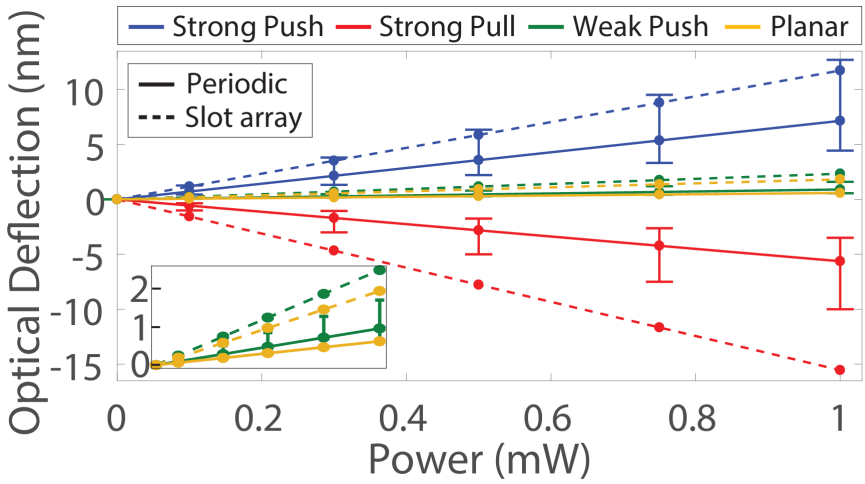

(b)

Figure 19. (a) Measured (solid circles) and fitted and predicted (lines) total deflection as a function of incident laser power: enhanced pushing force (blue), enhanced pulling force (red), weak pushing force (green), and planar surface (yellow). Inset: enlargement of the dashed square region showing measurement error bars. Dotted: fits to the measured data; dashed: fits from a simulation with a Gaussian beam incident on each slot array; and solid: fits from a simulation with plane wave illumination of the corresponding periodic structures using the measured mean slot width and period. (b) Extracted optical deflection: dashed lines are from the exact slot array structures; solid lines are from the periodic structure simulations. The error bars describe sensitivity to structure using the means and standard deviations of the slot arrays from the SEM images (and are not the extraction errors). The inset shows an expanded scale data. The blue curves for a large pushing force show about an order or magnitude increase in pressure relative to the planar surface (yellow).

those for each slot arrays with Gaussian beam illumination. All simulated results in Fig. 19(a) are sufficiently close to the measured data to make conclusions regarding extracted optical force deflection and related enhancement of the pressure.

The extracted optical deflection results as a function of incident optical power are shown in Fig. 19(b). The dashed lines are the results using the more accurate slice model with the measured Gaussian beam profile. The mean values of each slot width and separation for each array were obtained from the SEM images and used to obtain the simulated results (with the extracted α and β). The substantial differences between the large pushing force and pulling force deflections and the

planar results represent the force enhancement. In order to appraise sensitivity of the extraction to geometry variations, we pursued a statistical study, and those results are shown by the solid lines in Fig. 19(b) that have associated error bars. It should be emphasized that the resulting error bars are not the errors in determining the slot array parameters, but are in indication of sensitivity of the method for determining optical force deflection to gross variations in the geometry, should there have been factors of which we were unaware. From the SEM images, we obtained a mean and a standard deviation for each array slot width and period (see the caption of Fig. 16). Based on the geometry means and the means plus and minus the standard deviations, we calculated the optical force and power dissipation and repeated the least square fitting process with all the combinations of slot widths and separations for the different sets of slots, using the simple plane wave model. We determined the standard deviations of the fitted optical deflections and plot these as the error bars in Fig. 19(b). The error bars are asymmetric because the points and lines were determined using the geometry means, and the means from the statistical treatment are not identical. Note that even with this rather artificial and extreme set of variations in the extracted optical deflection, all results in Fig. 19(b) are distinct and clearly demonstrate an increase in deflection based upon slot structure, relative to the planar case. Importantly, Fig. 19(b) shows a force on the structured Au film, in the case of the large push force (blue), that is approximately an order of magnitude higher than that on the planar Au surface (yellow).

7.5 Conclusion

We have demonstrated an enhanced optical force on a metallic surface that depends on the nanostructured features. The increase in optical pressure therefore results from optical field interaction with the material in the third dimension. The general principle is that an asymmetric cavity-enhanced field increase, associated with a resonance, leads to an increase in the force density within the material and hence to a substantial increase in the total force, relative to the planar case. A negative pressure results from control of the scattered field in the structured material.

The interplay between material, structure at the nanometer-scale, and optical force will have substantial consequences in applications that include all-optical communication, remote actuation, propulsion, and biophysics. For example, in all-optical communication, optical signals could be used to move a structure that would then select a different optical (network) path [121, 122]. Remote actuation would be enhanced by greater sensitivity and control of the force direction, both of which might benefit cavity cooling [131, 132]. Regulation and enhancement of the optical force should prove interesting in the field of cavity optomechanics [133, 134]. Also, by structuring beads used in optical tweezer experiments related to biomolecules, more control during experiments to evaluate the influence of force and torque may be possible with patterned beads [102]. Finally, there has also been interest in thermomechanical structures, where light is used to heat and deform metal films [135].

8 Pushing and Pulling Optical Pressure Control with Plasmonic Surface Waves

8.1 Summary

We present an approach for pulling a passive nanostructured surface with light by establishing a transverse surface wave resonance, and the results are supported with numerical simulations of fields and force density in the material [136]. By applying a force density formulation from Einstein and Laub, pulling is achieved with a simple periodic array of slots in a gold film supporting a plasmon mode with single-plane-wave illumination. This can be understood as being due to excitation of a resonant field on the back that provides a dominant force density on the back of the gold film and hence pulling. In addition, an example metal-dielectric structure is presented that allows pushing or pulling, depending on wavelength and whether the surface wave on the front or the back dominates,

respectively. Similar to recent experimental results that showed a pressure greater than that on a perfect mirror is possible, both positive and negative pressures can exceed that on a planar mirror. This enhancement is due to a cavity resonance, in this case due to a transverse surface plasmon mode. This work motivates an experimental effort to demonstrate pulling with nanostructured media and offers a new paradigm in optomechanics.

8.2 Introduction

The interaction between light and materials has been widely studied. From Maxwell's picture, the maximum time-averaged radiation pressure is twice the incident time-averaged power density over the background light speed, which occurs on perfect mirror with a planar surface. We have demonstrated both experimentally [91] and interpreted this phenomenon by introducing an asymmetric cavity picture with an appropriate quality factor [90]. Recently, a statistical simulation study of aperiodic dielectric and metal elements provided example structures that could be pulled as well as pushed, with evidence of a relationship to the character of the resonances [103]. Lacking has been a simple explanation for pulling in relation to the geometry of the scattering structure. Evanescent fields from surface waves can provide resonant fields that can be controlled in interesting ways. We investigate this aspect by looking into plasmonic surface waves on a nanoslotted Au membrane. With the understanding of the relation between enhanced pressure and surface waves, one can then design structured metallic and dielectric materials where an increase in pressure over that on a perfect mirror is possible. One application domain is propulsion [137] (see Fig. 2).

To describe the optical force density inside the material due to the electromagnetic field, we utilize a formulation from Einstein and Laub [53]. The field solution is calculated by a finite element analysis, and then the force density and the corresponding collective normal pressure is obtained. The basic concept is that the incident light is coupled into a waveguide structure and the excited waveguide mode(s) facilitate control of the net force. Using relatively simple pictures, such as surface wave and MIM mode excitation [138–141], we can establish the underlying principles. Referring to (4), cavity resonances can result in an increase of both terms, but depending on the geometry, one may dominate. In the case of plasmon surface waves, it is the metal-insulator and metal-insulator-metal (MIM, slot) modes that are of interest.

8.3 Slots in a Gold Film

We investigate opportunities for both pushing and pulling of a An membrane having a periodic array of slots. Figure 20(a) shows the simulation arrangement for a periodic structure composed of a gold (Au) film with a single slot in each period, Λ, where W is the slot width and T is the gold thickness. A plane wave is incident from the top with $\mathbf{H}$ polarized out of the page, a wavelength of 633 nm, and an intensity equivalent to 1 mW over 1μm circular radius circle. The corners of the geometry are rounded with a 2 nm quarter circle to avoid issues with singular fields. With the incident field having $\mathbf{H} = \hat{\mathbf{z}}H$, surface plasmon modes are excited at the metal-vacuum interfaces, and in the slot, a metal-insulator-metal (MIM) mode exists [140]. Fixing W at 60 nm, Λ was varied to find the transverse resonance condition for the front and back plasmon modes (at the Au-vacuum interfaces). The resonant condition was found to be $\Lambda = 620$ nm, which is close to the plasmon surface wave wavelength [142]. Fixing both W (60 nm) and Λ (620 nm) and varying T, we find the pressure varies as in Fig 20(b). The dashed black line is zero pressure and positive pressures indicate pulling because the the plane wave is incident from the top in the $-y$-direction. The dashed red line indicates the pressure on the perfect mirror with the same incident field intensity. Figure 20(c) plots the calculated power density on the back side of the Au membrane with respect to T, showing resonant coupling through the slot MIM mode. Comparing Figs. 20(b) and (c), we see that a pulling pressure is promoted when the power density on the back side of the Au

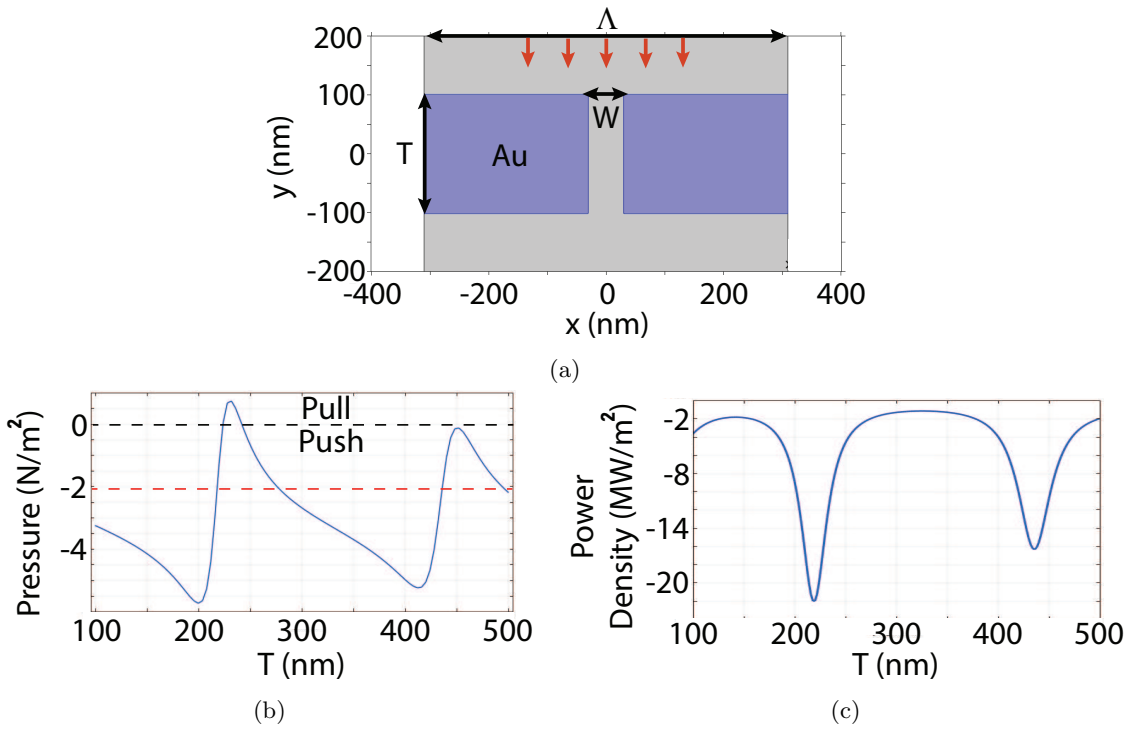

Figure 20. (a) Simulation setup of a cut-through slotted Au membrane, where Λ is the period, W is the slot width, and T is the gold thickness. The plane wave incident from the top is polarized with **H** out of the page, the wavelength is 633 nm, and the intensity is equivalent to 1 mW over a 1μm circular radius spot. (b) The calculated pressure when Λ=620 nm and W=60 nm, with the Au film thickness (T) varied from 100 nm to 500 nm. The red dashed line indicates the pressure on a perfect mirror with the same incident field intensity. The region above the black dashed line is the pulling pressure regime and below this line the pushing pressure region, because the plane wave is incident from the top and in the $-y$-direction. (c) The calculated power density on the bottom side of the Au film, with respect to the Au thickness. The peaks correspond to situations where the metal-insulator-metal (MIM) mode in the slot provides resonant transfer through the film. Comparing (b) and (c), we can see that a pulling pressure peak coincides with significant coupling to the back of the film and hence resonant coupling through the slot.

membrane has its largest magnitude, indicating coupling of the incident field through to the back. The resonant features in Figs. 20(b) and (c) are separated by half a wavelength for the lowest order MIM mode. The effective excitation of the back surface wave is associated with coupling light through the structure that results in a recoil force in the direction opposite to that of the incident light.

Now consider the field and force density solutions shown in Fig. 21 in the neighborhood of T = 200 nm in Fig. 20(b), where the largest pushing and pulling pressures occur. The largest pushing pressure (left column of Fig. 21) of -5.77 N/m^2 occurs at T = 203 nm and is about 3 times greater than that on a perfect mirror. Increasing T to 232 nm results in a change to a pulling pressure (right column of Fig. 21) of 0.77 N/m^2. Figures 21(a) and (b) show the x-directed electric field magnitude and that an MIM resonant mode is developed in the slot cavity. This resonant MIM mode excites the surface wave on the front and back of the Au, as shown in Figs. 21(c) and (d), indicated here by the dominant y-component of the electric field. The calculated time-averaged y-directed force density (N/m^3) is shown in Figs. 21(e) and (f), where blue is a pushing force density and red is a pulling force density. In Fig. 21(c) and (e), a larger surface wave is developed on the front of the Au, resulting in larger pushing force density and an enhanced pushing pressure. However, in Figs. 21(d) and (f), a larger surface wave amplitude, and as a result a larger pulling force density, is developed on the back of the Au film, resulting in a pulling pressure. From the two cases, the surface waves on the top and the bottom of the Au film compete with each other

and therefore decrease the net magnitude of the collective pressure. We conclude that the pressure could be enhanced if the surface wave at the top (for pulling) or the bottom (for pushing) can be suppressed.

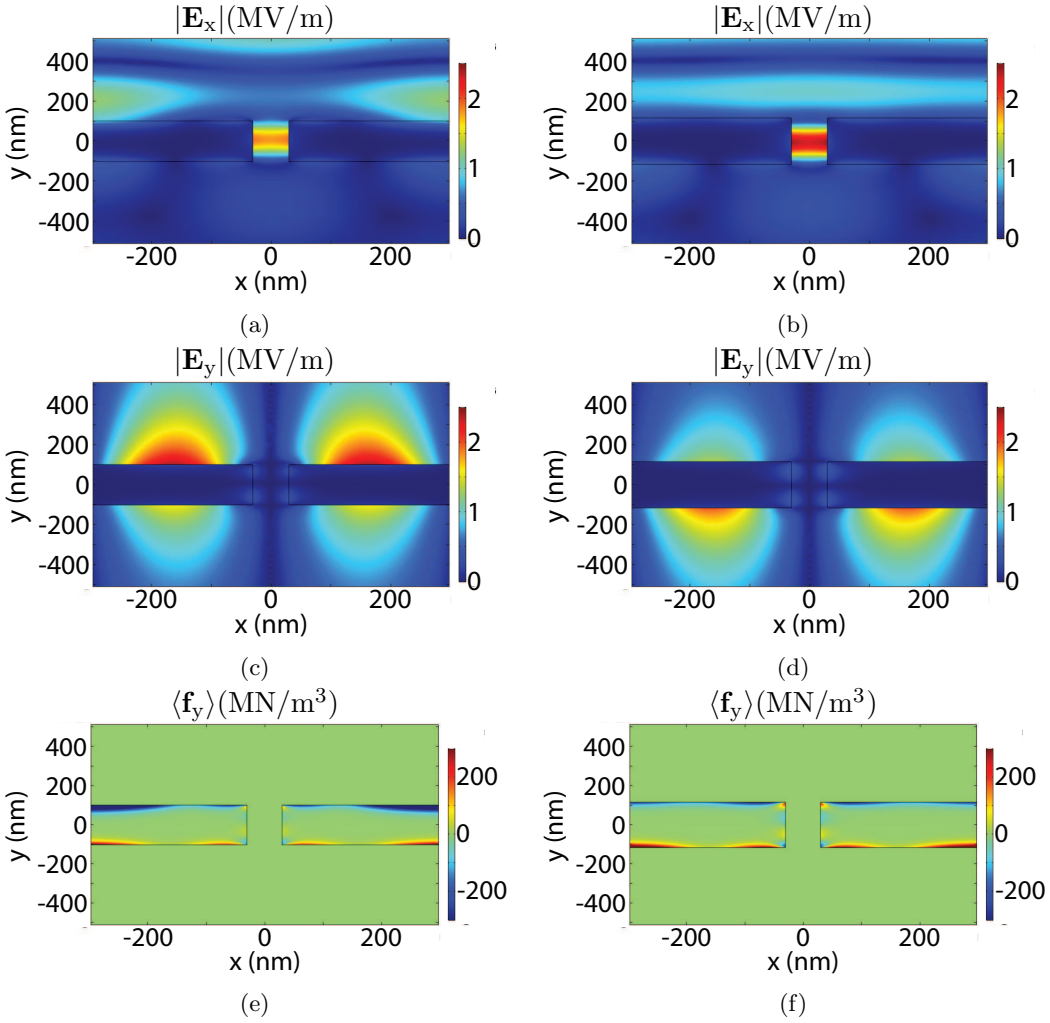

Figure 21. Simulation results for the largest pushing pressure ((a), (c), and (e)) with $T = 203$ nm and the adjacent pulling pressure situation ((b), (d), and (f)) with $T = 232$ nm, referring to Fig. 20(b). (a) and (b): $|\mathbf{E}_x|$, clearly showing the slot MIM mode resonance. (c) and (d): $|\mathbf{E}_y|$, showing the front and back surface waves. (e) and (f): Time-averaged y-directed force density (N/m^3). The MIM mode in (a) and (b) promotes the top (incident field side) and bottom resonant surface waves seen in (c) and (d). In (e), the pushing force density on the top Au surface dominates, resulting in enhanced pushing pressure of -5.77 N/m^2, while in (f) the more substantial pulling force density associated with the surface wave on the bottom of the Au film results in the small pulling of 0.77 N/m^2.

8.4 Pushing and Pulling with a Gold-Dielectric Film Structure

One approach to regulate the surface wave is to modify the resonance condition by control of the mode phase constant through a dielectric film. We consider a Au film with a periodic array of slots and a dielectric film on the top and/or the bottom, as in Figs. 22 and 23. Such an arrangement could be fabricated on an SiN membrane, as we did previously [91]. In each case, a plane wave is incident from the top with magnetic field out of the page. By regulating the parameters, we show that a dominant surface wave on the top (front) results in a pushing force, and when a strong

surface wave is on the bottom (back) of the structure, a pulling force. A strong front or back surface wave occurs with transverse resonance, and coupling through to the back with resonance of the metal-insulator-metal slot mode.

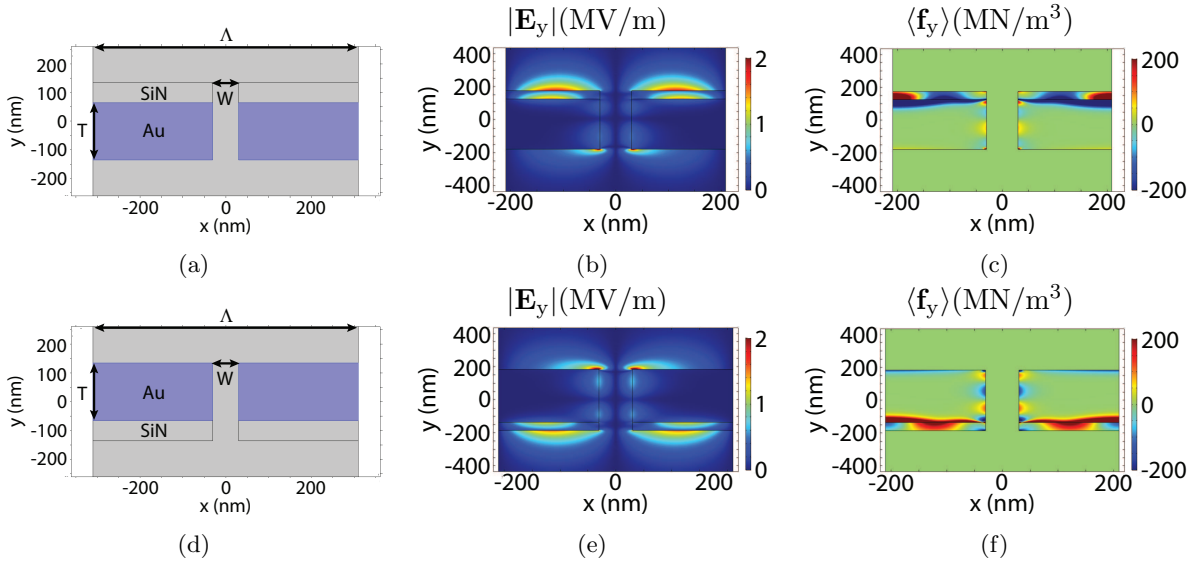

Figure 22. Simulation of a periodic nanostructured Au membrane with a SiN layer ($n = 2$ at 633 nm) added to the top ((a)-(c)) or bottom ((d)-(f)) of a Au film. A 633 nm plane wave is normally incident from the top with magnetic field out of page, and the power density is equivalent to 1 mW over 1 μm radius circle. Parameters: period Λ, slot width W, and Au thickness T, Au dielectric constant $\epsilon_{\rm Au} = -11.8 + i1.23$ (633 nm). (a) and (d) simulated structures with a SiN film on the top and bottom, respectively, with (a) period Λ=418 nm, slot width W=60 nm, Au thickness T=304 nm, and SiN thickness 50 nm; and (d) Λ=420 nm, W=60 nm, T=320 nm, and SiN thickness 50 nm. The corresponding y-directed electric field magnitudes are shown in (b) and (e). The y-directed time-averaged force densities are shown in (c) and (f). The top row shows the case of an enhanced pushing pressure of 20.3 N/m^2 and the bottom row a pulling pressure of 10.12 N/m^2. The pushing pressure magnitude on a perfect mirror with the same intensity is 2.12 N/m^2.

Figures 22(a) and (d) show the simulation setup with a 50 nm SiN layer added to the front or back of a Au membrane, respectively. A 633 nm plane wave is normally incident from the top and the intensity is equivalent to 1 mW over a 1 μm radius circle. The corresponding pushing pressure on the perfect mirror is 2.12 N/m^2. The top row of Fig. 22 presents the case of an enhanced pushing pressure and the bottom row shows the situation with an enhanced pulling pressure. Figures 22(b) and (e) show the magnitudes of the corresponding y-directed electric fields, dominant in the transverse surface (plasmon) wave. Figures 22(c) and (f) show the calculated time-averaged y-directed (normal component) force density. With the SiN layer on the top (Figs. 22(a)-(c)), we find a pushing pressure of 20.3 N/m^2 (period of Λ=418 nm, Au thickness of T=304 nm, and slot width of W=60 nm). From Fig. 22(b), the resonant mode is promoted on the top surface and the interaction of the field with the Au and the SiN film produces the enhanced pushing force density on the top (front) in Fig. 22(c). For the case with the SiN layer on the bottom (back, Figs. 22(d)-(f)), we find an enhanced pulling pressure of 10.12 N/m^2 (Λ=460 nm, W=60 nm, and T=320 nm). From Fig. 22(e), we see that the top surface wave is diminished due to the change of the transverse resonance condition (Λ) and Fig. 22(f) shows that the pulling force density on the back of the membrane dominates.

We show that it is possible to achieve either a pushing or a pulling pressure with the same structure by tuning the incident field wavelength. Figure 23(a) describes the simulated structure, where Λ=460 nm, W=60 nm, and T=306 nm. A 10 nm-thick dielectric layer is added to the top with a refractive index of 1.5, 2, and 2.5, and the back SiN thickness is 40 nm. The refractive index of both dielectric films is assumed independent of wavelength in this example (and a value

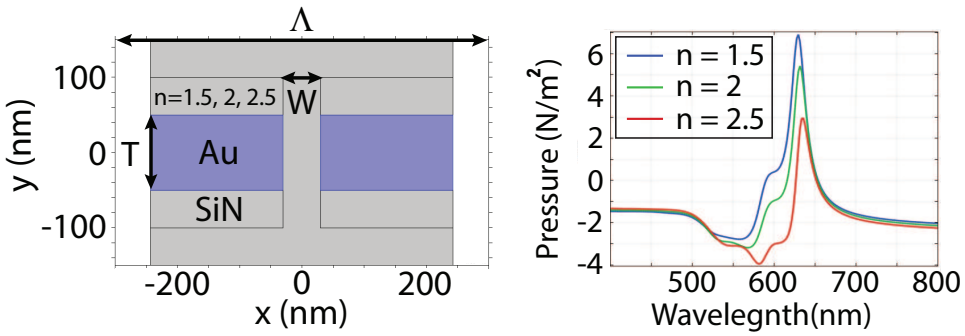

(a) (b)

Figure 23. Simulation of wavelength-controlled pushing/pulling pressure on a periodic nanostructured SiN-Au-SiN membrane. The illuminating wave condition is the same as in Fig. 22. (a) Simulation setup with parameters: period Λ=460 nm, slot width W=60 nm, Au thickness T=306 nm, top dielectric thickness 10 nm, with refractive indices $n = 1.5, 2, 2.5$, and bottom SiN thickness 40 nm. (b) Calculated time-averaged y-directed pressure with the incident wavelength varied from 400 nm to 800 nm: blue, $n = 1.5$; green, $n = 2$; red, $n = 2.5$. A positive value indicates a pulling pressure and a negative value a pushing pressure (light is incident from the top in the $-y$-direction). An enhanced pushing pressure is developed around 570 nm and the enhanced pulling pressure in the neighborhood of 630 nm.

of 2 was used for SiN). The wavelength-dependent dielectric constant of Au is used [61]. The illuminating wave condition is the same as in Fig. 22. Figure 23(b) shows the calculated time-averaged normal pressure with an incident wavelength varying from 400 nm to 800 nm, for the three different refractive indices of the top dielectric layer. A positive value indicates a pulling pressure while a negative value indicates a pushing pressure (the light is incident from the top and in the $-y$-direction). Note that a pushing pressure occurs with an incident field wavelength around 570 nm and a pulling pressure when the wavelength is in the neighborhood of 630 nm, and for the $n = 2.5$ case (red curve), the pushing and pulling pressure magnitudes are approximately equal at these two wavelengths.

Our results show that simple structures can be designed to be pushed and pulled by light. This phenomenon occurs due to the excitation of field resonances and these can be regulated by design. It thus appears possible to regulate both the magnitude and direction of the net optical pressure on a nanostructured material.

9 Experiment for Measuring Deflection of a Membrane

We built a new and sensitive experiment to accurately measure the deflection of a membrane and hence determine whether it is possible to pull a structure with a simple laser beam. This experiment, presented schematically in Fig. 24, involves laser-driven deflection of a SiN membrane with a patch of Au deposited on top and slot arrays etched through both the Au and SiN. When illuminated by a force laser, the optical force will deflect the membrane. This deflection will be measured by a quadrant detection system.

Due to the differing thermal properties of Au and SiN, the Au patch could expand at a different rate than the bulk membrane. This expansion would introduce a strain that tends to pull the Au away from the SiN, leading to buckling of the membrane. To demonstrate true pulling and eliminate thermal buckling as the cause of deflection, the experiment will be repeated with the membrane illuminated on both the Au and SiN sides. Based on simulation results the former will result in a larger and hence easier to measure deflection. The latter will orient the pulling force such that it acts in opposition to the buckling, leaving the optical force as the only cause of the pulling.

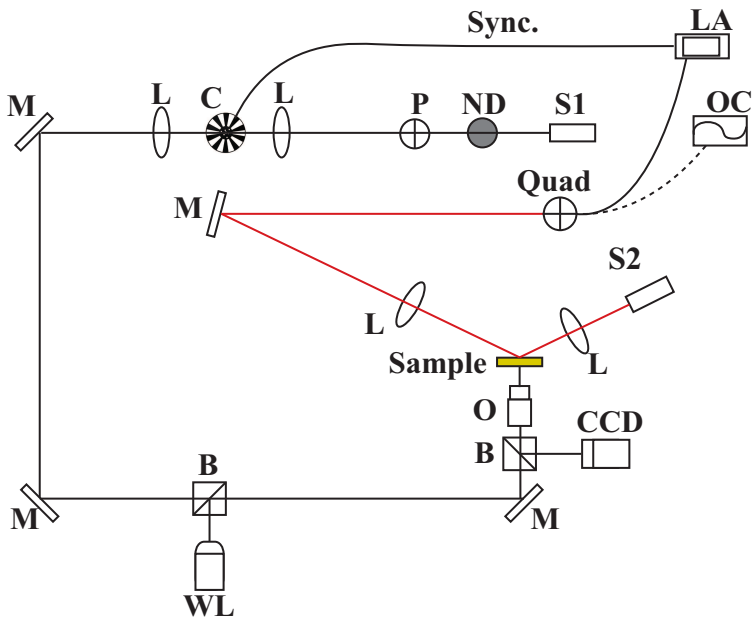

Figure 24. Schematic for the experiment: force laser (S1), sensing laser (S2), quadrant photodiode with bandpass filter (Quad), oscilloscope (OC), lock-in amplifier (LA), neutral density filter (ND), white light source (WL), polarizer (P), chopper (C), objective lens (O), silver mirror (M), beam splitter (B), lens (L), charge coupled device (CCD) camera. The membrane structure location will be adjusted using a computer-controlled system of motorized stages.

10 Design and Fabrication Nanostructured Membranes

Our intent is to fabricate nanostructures on SiN membranes with Au patches using focused ion beam (FIB) milling in Purdue's Birck Nanotechnology Center (BNC). The SiN membranes we have used in our experimental work came from Norcada, a MEMS technology company based in Edmonton, Alberta, Canada. We learned that Norcada has the capacity to fabricate slot arrays in SiN membranes with Au patches having modest slot widths (100 nm), and for a reasonable cost. We worked with Norcada to define a fabrication effort and iterated on structure design features that incorporated specific geometries related to the process they can employ, and those structured membranes have been received and will be used in experimental studies related to motion control with optical force.

11 Pulling Pressure with All-Dielectric Materials

11.1 Summary

We consider simple all-dielectric arrangements that provide a pulling pressure and hence a net negative force results. The simulations described should lead to an interesting set of experiments, and relate to various applications.

11.2 Introduction

We have presented various metal and metal-dielectric structures that offer pushing and pulling pressures through regulation of resonant modes. This allows control of the direction by varying the parameters associated with the incident field. Metals offer strong scatter and provide for surface waves and very small optical cavities, and were used to show enhanced pressure effects. Resonant-based dielectric structures can behave similarly, and results from an aperiodic binary material system support this [103]. However, the use of metals will also have accompanying heating [91], so

that the optomechanics cannot simply be regulated by the optical force. While this thermomechanical deflection may be useful in some situations, in some applications all-dielectric structures may be preferable. One example would be Si photonics, where waveguides are formed in Si. We have learned that regulation of the resonances in structured dielectrics can provide for pushing or pulling [103]. However, simple dielectric arrangements, such as films, would be useful in applications. This leads us to consider pulling forces with dielectric films.

We discovered from our earlier work [54] that a thin, low dielectric constant film in a higher dielectric constant background experiences a negative force from the analytic solution for the fields and force density. This makes the three-layer dielectric system with a low dielectric constant film sandwiched in higher dielectric constant layers interesting to study. On the other hand, the second term in (4) reveals that with a positive dielectric constant, a pulling force can be established with an evanescent field. That is, the gradient force can provide the condition needed for pulling. One simple way to establish an evanescent field is from internal total reflection, when light incident from a high dielectric constant region onto a low dielectric constant region above the critical angle. These two strategies are straightforward and easy to fabricate. We consider Si and SiN in our simulations because they are widely employed.

11.3 Pulling Force with Low-Dielectric Constant Film in a Higher Dielectric Constant Background

We might consider that a low dielectric constant film sandwiched between semi-infinite high dielectric constant regions (the three-region problem [54]) has a practical incarnation as three slabs, where the thicknesses of the outer two are adjusted so as to have no net force in those regions. However, this implies adequate degrees of freedom for this operating condition. By way of illustration, a single film with negligible dissipation has no net force when it is an integer multiple of half a wavelength thick [54]. Therefore, by tuning the parameters of the high dielectric constant slabs, and assuming a fixed laser wavelength, we anticipate realizing a pulling force on the composite. Thus, by changing the angle of incidence or the wavelength, pushing would result. This structure could be easily fabricated on a SiN membrane by coating both sides with Si. Figure 25 shows the simulation results. A plane wave with magnetic field out of page is normally-incident from a semi-infinite high refractive index (the top, $n = 4$) material to a low refractive index ($n = 2$) film with a free space wavelength of 633 nm and an intensity corresponding to 1 mW over 1 μm radius circle. The simulation setup is shown in Fig. 25(a), where T is the thickness of the $n = 2$ layer. We calculate the pressure on $n = 2$ layer by varying T. Figures 25(b) and (c) show the electric field standing wave in the film for thicknesses of quarter and half a wavelength, respectively, the cases for maximum and minimum (zero) force on the slab. In Fig. 25(d), the pressure on the film is plotted as a function of the thickness of the low dielectric constant slab. Figure 25(e) gives the time-averaged y (normal) component of the force density as a function of distance in the slab for a thickness corresponding to a quarter of a wavelength, and Fig. 25(f) shows the force density when the thickness is half a wavelength. The largest pulling pressure occurs when $T = (2m + 1)\lambda_{n=2}/4$ and zero pressure occurs when $T = (2m+1)\lambda_{n=2}/2$, where $m = 0, 1, 2, ...$ Here, the pulling pressure is positive because the wave is incident from the top and in the $-y$ direction. The challenge is to find a situation where the total pressure on a structure with finite dielectric thicknesses provides pulling. This result also has fundamental implications in relation to the interaction of photons in material and the underlying theory. This work is being expanded and will be submitted for publication.

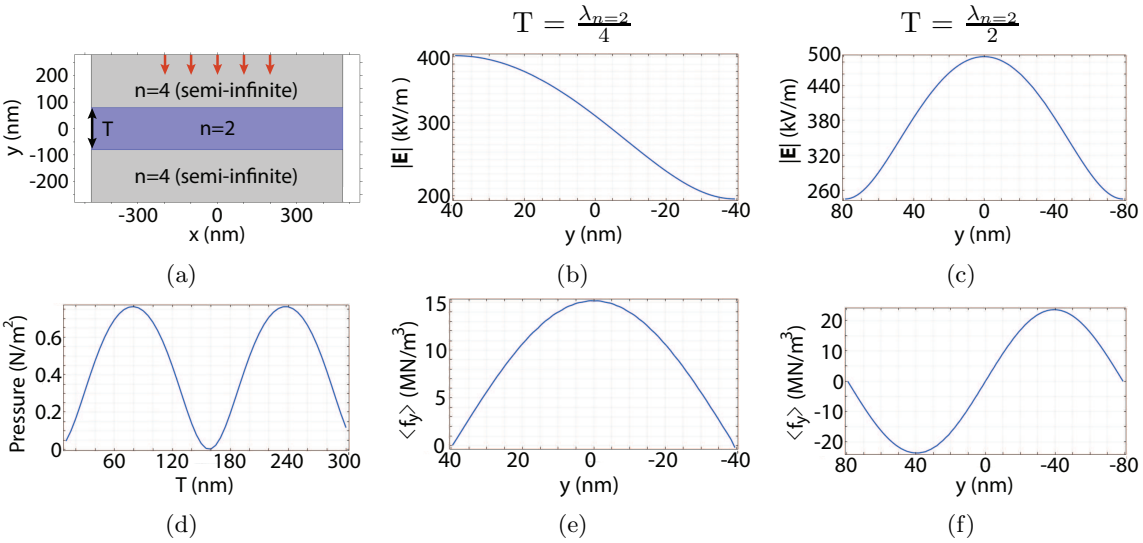

Figure 25. Simulation of a normally-incident plane wave (magnetic field out of the page) from a semi-infinite high refractive index ($n = 4$) material to low refractive index ($n = 2$) film with a free space wavelength of 633 nm. The intensity corresponds to 1 mW over 1 μm radius circle. (a) Simulation setup, where T is the thickness of the $n = 2$ layer. (d) Calculated pressure in the $n = 2$ region with varying T. A pulling pressure is positive because the wave is incident from the top. (b) and (e): Calculated electric field magnitude and time-averaged y-directed force density, respectively, in the $n = 2$ region when $T = \lambda_{n=2}/4$. (c) and (f): Calculated electric field magnitude and time-averaged y-directed force density, respectively, in the $n = 2$ region when $T = \lambda_{n=2}/2$. When the electric field solution is asymmetric we have non-compensated pulling force density.

11.4 Pulling Force with Internal Total Reflection

With light incident from a high dielectric constant region onto a low dielectric constant region above the critical angle, an evanescent (decaying) field results in the low dielectric constant region. This can be achieved in a waveguide geometry and by coupling light with a few grating periods formed in the dielectric. Figure 26(a) shows the electric field magnitude (with magnetic field out of the page) with oblique incidence from a region with refractive index (n) 4 to a film with refractive index 2, showing the evanescent field in this region. The resulting pressure determined from (4) for the $n = 2$ region is shown in Fig. 26(b), with the separation of the terms: cross is the first term in (4) and gradient is the second. Notice from Fig. 26(b) that there is a range of incident angles (in the neighborhood of and beyond the critical angle) where the pressure is positive, indicating pulling, and a region where there is a pushing force. This arrangement is promising for implementation on a SiN membrane.

12 Force on a Planar Mirror

Realizing optomechanical devices from nanostructured media requires a spatially-dependent force density model in the material. The general Einstein-Laub force density has been shown to be consistent with a boundary description, thereby completing a needed analytic description. This work has been submitted as a conference paper (2022 Optica/APS/IEEE CLEO).

We have theoretical work that compares the common Maxwell picture of pressure on a mirror [35, 59] to the result with application of the Einstein and Laub force formulation [51, 53, 55]. This is done by applying the two different force formulations to the same theoretical situation of a plane wave normally incident on a planar mirror with varying material parameters. In the case of a simple semi-infinite planar mirror, we have derived an analytical expression for the time-average pressure on the mirror with monochromatic light, starting from the force density in (10), in the case of a

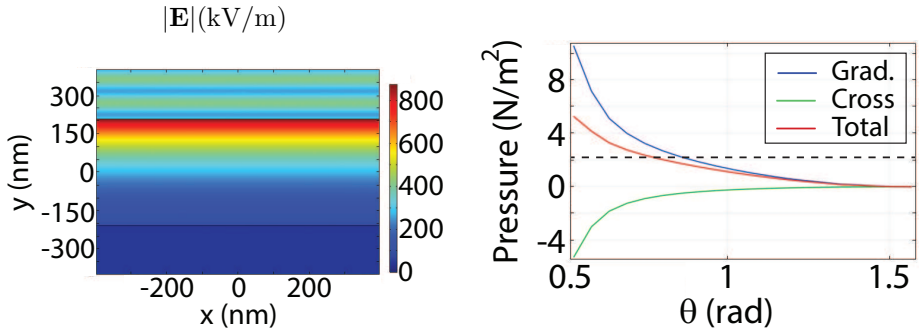

(a) (b)

Figure 26. Simulation of an obliquely-incident plane wave (magnetic field out of the page) from a high refractive index ($n = 4$) material to low refractive index ($n = 2$) film ($-200 \leq y \leq 200$ nm) with a free space wavelength of 633 nm and an intensity corresponding to 1 mW over 1 μm radius circle. (a) Electric field magnitude, showing the evanescent field in the $n = 2$ film. (b) Calculated gradient pressure from the second term in (4) (blue curve), Poynting-like pressure from the first, cross term of (4) (green curve), and the total pressure (red curve) on the low refractive index material. The black dashed line is corresponding pushing pressure magnitude on a perfect mirror. Note that there is a pulling force for smaller angles (beyond the critical angle) and a pushing force for large angles, allowing the direction of the force to be adjusted with angle.

normally incident plane wave. We also showed that the same expression results from application of (6). The result holds for all semi-infinite medium parameters and in the case of a normally incident plane wave. Because of the varying origins and derivations of the two expressions, we sought to compare their results in a simple situation with important physical meaning. The case of a plane wave on a semi-infinite planar mirror has many implications as an approximation over a small region of material.

13 Broader Impacts

13.1 Science

Our research has fundamental implications related to optical forces in materials and how to consider the mechanical aspects of photons. This is of broad consequence in science and engineering, and our work involves key steps to clarify the mechanical attributes of electromagnetic waves and fields in materials, which has remained rather mysterious despite advancements in other related fields during the past century. The uses of nanostructured materials in new technology is illustrated through several examples in Fig. 2. Our work to pull a structure with a simple laser beam and to push with large force using asymmetric cavity enhancement are enabling optomechanical system concepts.

13.2 Graduate Students and Education

Graduate students Adam Behnke and Tom Pollei worked on this project most recently, and this research will constitute their Ph.D. theses. Dr. Li-Fan Yang completed his Ph.D. in 2020 and his thesis was focused on experimental and simulation-based aspects of optomechanics in nanostructured media (Optical Force Regulation with Nanostructured Materials). Dr. Yu-Chun Hsueh completed his Ph.D. in 2018 (Field Control and Optical Force Enhancement in Aperiodic Nanostructures).

Two undergraduate students were involved in this research. Jackson Gihl, a Purdue undergraduate student in the School of Electrical and Computer Engineering (ECE), worked with the Webb group under an National Science Foundation REU award. In addition, Scott Kenning, a Purdue ECE undergraduate student, has been working on modeling of membrane mechanics with

laser illumination. This is relevant to understanding membrane motion in experiments and the extraction of optical force information.

14 Publications

The following papers associated with this award have been published, recently presented, and submitted, or are in preparation.

1. A. H. Velzen and K. J. Webb, "Electromagnetic force on structured metallic surfaces," Phys. Rev. B **92**, 115416 (2015).

2. K. J. Webb, "Relationship between the Einstein-Laub electromagnetic force and the Lorentz force on free charge," Phys. Rev. B **94**, 064203 (2016).

3. Y.-C. Hsueh, L.-F. Yang, and K. J. Webb, "Enhanced optical pressure with asymmetric cavities," Phys. Rev. B **99**, 045437 (2019).

4. Y.-C. Hsueh, L.-F. Yang, and K. J. Webb, "Optical pressure control with aperiodic nanostructured material," J. Opt. Soc. Am. B **36**, 1408-1419 (2019).

5. L.-F. Yang, A. Datta, Y.-C. Hsueh, X. Xu, and K. J. Webb, "Demonstration of enhanced optical pressure on a structured surface,' 'Phys. Rev. Lett. **122**, 083901 (2019).

6. K. J. Webb (*Invited*), L.-F. Yang, A. Datta, Y.-C. Hsueh, and X. Xu, "Enhanced optical force with nanostructured material," The 50th Winter Colloquium on the Physics of Quantum Electronics, Snowbird, UT, Jan. 5-10, 2020.

7. L.-F. Yang and K. J. Webb, "Pushing and pulling optomechanics with plasmonic surface waves," OSA/IEEE/APS CLEO (Conference on Lasers and Electrooptics) Meeting, San Jose, CA, May 11-15, 2020 (moved to a virtual on-line meeting): Digest paper for Presentation FM4Q.3.

8. L.-F. Yang and K. J. Webb, "Pushing and pulling optical pressure control with plasmonic surface waves," Phys. Rev. B **103**, 245124 (2021).

9. T. J. Pollei, A. W. Behnke, and K. J. Webb, "Einstein-Laub force on a mirror," In preparation and 2022 Optica/APS/IEEE CLEO conference submission.

15 References

[1] A. Ashkin, J. M. Dziedzic, J. E. Bjorkholm, and S. Chu, "Observation of a single-beam gradient force optical trap for dielectric particles," Opt. Lett. **11**, 288–290 (1986).

[2] D. G. Grier, "A revolution in optical manipulation," Nature **424**, 810–816 (2003).

[3] L. P. Ghislain, N. A. Switz, and W. W. Webb, "Measurement of small forces using an optical trap," Rev. Sci. Instrum. **65**, 2762–2768 (1994).

[4] A. Rohrbach and E. H. K. Stelzer, "Trapping forces, force constants, and potential depths for dielectric spheres in the presence of spherical aberrations," Appl. Opt. **41**, 2494–2507 (2002).

[5] R. I. Litvinov, H. Shuman, J. S. Bennett, and J. W. Weisel, "Binding strength and activation state of single fibrinogen-integrin pairs on living cells," Proc. Natl. Acad. Sci. **99**, 7426–7431 (2002).

[6] F. Gittes and C. F. Schmidt, "Signals and noise in micromechanical measurements," Meth. Cell Biol. **55**, 129–156 (1997).

[7] F. Gittes and C. F. Schmidt, "Interference model for back-focal-plane displacement detection in optical tweezers," Opt. Lett. **23**, 7–9 (1998).

[8] A. Pralle, M. Prummer, E. L. Florin, E. H. Stelzer, and J. K. Hörber, "Three-dimensional high-resolution particle tracking for optical tweezers by forward scattered light," Microsc. Res. Techniq. **44**, 378–386 (1999).

[9] A. Ashkin, "History of optical trapping and manipulation of small-neutral particle, atoms, and molecules," IEEE J. Sel. Top. Quant. Electron. **6**, 841–856 (2000).

[10] K. Svoboda, P. P. Mitra, and S. M. Block, "Fluctuation analysis of motor protein movement and single enzyme kinetics," Proc. Natl. Acad. Sci. **91**, 11782–11786 (1994).

[11] C. Bustamante, S. B. Smith, J. Liphardt, and D. Smith, "Single-molecule studies of dna mechanics," Curr. Opin. Struct. Biol. **10**, 279–285 (2000).

[12] A. H. Yang, S. D. Moore, B. S. Schmidt, M. Klug, M. Lipson, and D. Erickson, "Optical manipulation of nanoparticles and biomolecules in sub-wavelength slot waveguides," Nature **457**, 71–75 (2009).

[13] G. Wright, M. J. Tucker, P. C. Morton, C. Sweitzer-Yoder, and S. E. Smith, "Micromanipulation in assisted reproduction: A review of current technology," Curr. Opin. Obstet. Gynecol. **10**, 221–226 (1998).

[14] J. C. Crocker and D. G. Grier, "Microscopic measurement of the pair interaction potential of charge-stabilized colloid," Phys. Rev. Lett. **73**, 352–355 (1994).

[15] J. C. Crocker and D. G. Grier, "When like charges attract: the effects of geometrical confinement on long-range colloidal interactions," Phys. Rev. Lett. **77**, 1897–1900 (1996).

[16] Y. N. Ohshima, H. Sakagami, K. Okumoto, A. Tokoyoda, T. Igarashi, K. B. Shintaku, S. Toride, H. Sekino, K. Kabuto, and I. Nishio, "Direct measurement of infinitesimal depletion force in a colloid-polymer mixture by laser radiation pressure," Phys. Rev. Lett. **78**, 3963–3966 (1997).

[17] J. C. Crocker, J. A. Matteo, A. D. Dinsmore, and A. G. Yodh, "Entropic attraction and repulsion in binary colloids probed with a line optical tweezer," Phys. Rev. Lett. **82**, 4352–4355 (1999).

[18] R. Verma, J. C. Crocker, T. C. Lubensky, and A. G. Yodh, "Attractions between hard colloidal spheres in semiflexible polymer solutions," Macromolecules **33**, 177–186 (2000).

[19] A. G. Yodh, K. Lin, J. C. Crocker, A. D. Dinsmore, R. Verma, and P. D. Kaplan, "Entropically driven self–assembly and interaction in suspension," Phil. Trans. R. Soc. A **359**, 921–937 (2001).

[20] G. M. Wang, E. M. Sevick, E. Mittag, D. J. Searles, and D. J. Evans, "Experimental demonstration of violations of the second law of thermodynamics for small systems and short time scales," Phys. Rev. Lett. **89**, 50601 (2002).

[21] M. L. Juan, M. Righini, and R. Quidant, "Plasmon nano-optical tweezers," Nature Photon. **5**, 349–356 (2011).

[22] R. Quidant, D. Petrov, and G. Badenes, "Radiation forces on a rayleigh dielectric sphere in a patterned optical near field," Opt. Lett. **30**, 1009–1011 (2005).

[23] C. C. DuFort, M. J. Paszek, and V. M. Weaver, "Balancing forces: architectural control of mechanotransduction," Nature Rev. Mol. Cell Biol. **12**, 308–319 (2011).

[24] N. Wang, J. P. Butler, and D. E. Ingber, "Mechanotransduction across the cell surface and through the cytoskeleton," Science **260**, 1124–1127 (1993).

[25] M. Dienerowitz, M. Mazilu, and K. Dholakia, "Optical manipulation of nanoparticles: a review," J. Nanophotonics **2**, 021875–021875 (2008).

[26] M. Povinelli, M. Ibanescu, S. G. Johnson, and J. Joannopoulos, "Slow-light enhancement of radiation pressure in an omnidirectional-reflector waveguide," Appl. Phys. Lett. **85**, 1466–1468 (2004).

[27] D. Woolf, M. Loncar, and F. Capasso, "The forces from coupled surface plasmon polaritons in planar waveguides," Opt. Express **17**, 19996–20011 (2009).

[28] V. Liu, M. Povinelli, and S. Fan, "Resonance-enhanced optical forces between coupled photonic crystal slabs," Opt. Express **17**, 21897–21909 (2009).

[29] A. N. Grigorenko, N. W. Roberts, M. R. Dickinson, and Y. Zhang, "Nanometric optical tweezers based on nanostructured substrates," Nature Photon. **2**, 365–370 (2008).

[30] M. Righini, G. Volpe, C. Girard, D. Petrov, and R. Quidant, "Surface plasmon optical tweezers: tunable optical manipulation in the femtonewton range," Phys. Rev. Lett. **100**, 186804 (2008).

[31] B. J. Roxworthy, K. D. Ko, A. Kumar, K. H. Fung, E. K. Chow, G. L. Liu, N. X. Fang, and K. C. Toussaint Jr, "Application of plasmonic bowtie nanoantenna arrays for optical trapping, stacking, and sorting," Nano Lett. **12**, 796–801 (2012).

[32] B. J. Roxworthy and K. C. Toussaint Jr, "Femtosecond-pulsed plasmonic nanotweezers," Sci. Rep. **2** (2012).

[33] W. Zhang, L. Huang, C. Santschi, and O. Martin, "Trapping and sensing 10 nm metal nanoparticles using plasmonic dipole antennas," Nano Lett. **10**, 1006–1011 (2010).

[34] K. Wang, E. Schonbrun, P. Steinvurzel, and K. B. Crozier, "Trapping and rotating nanoparticles using a plasmonic nano-tweezer with an integrated heat sink," Nat. Comm. **2**, 469 (2011).

[35] E. F. Nichols and G. F. Hull, "The pressure due to radiation," Phys. Rev. **17**, 26–50 (1903).

[36] P. Penfield and H. A. Haus, *Electrodynamics of Moving Media* (MIT Press, Cambridge, MA, 1967).

[37] L. J. Chu, H. A. Haus, and P. Penfield, "The force density in polarizable and magnetizable fluids," Proc. IEEE **54**, 920–935 (1966).

[38] J. P. Gordon, "Radiation forces and momenta in dielectric media," Phys. Rev. A **8**, 14–21 (1973).

[39] I. Brevik, "Experiments in phenomenological electrodynamics and the electromagnetic energy-momentum tensor," Phys. Rep. **52**, 133–201 (1979).

[40] R. Loudon, S. M. Barnett, and C. Baxter, "Radiation pressure and momentum transfer in dielectrics: The photon drag effect," Phys. Rev. A **71**, 063802 (2005).

[41] R. N. C. Pfeifer, T. A. Nieminen, N. R. Heckenberg, and H. Rubinsztein-Dunlop, "Momentum of an electromagentic wave in dielectric media," Rev. Mod. Phys. **79**, 1197–1216 (2007).

[42] R. V. Jones and B. Leslie, "The measurement of optical radiation pressure in dispersive media," Proc. Royal Soc. A **360**, 347–363 (1978).

[43] R. V. Jones and J. C. S. Richards, "The pressure of radiation in a refracting medium," Proc. Royal Soc. A **221**, 480–498 (1954).

[44] M. Abraham, "Zur elektrodynamik bewegter körper," Rend. Circ. Mat. Palermo **28**, 1–28 (1909).

[45] M. Abraham, "Sull'elettrodinamica di minkowski," Rend. Circ. Mat. Palermo **30**, 33–46 (1910).

[46] H. Minkowski, "Die grundgleichungen für die elektromagnetischen vorgänge in bewegten körpern," Nachr. Ges. Wiss. Göttingen Math.-Phys. Kl. pp. 53–111 (1908).

[47] H. Minkowski, "Die grundgleichungen für die elektromagnetischen vorgänge in bewegten körpern," Math. Ann. **68**, 472–525 (1910).

[48] R. V. Jones, "Radiation pressure of light in a dispersive medium," Proc. Royal Soc. A **360**, 365–371 (1978).

[49] J. C. Garrison and R. Y. Chiao, "Canonical and kinetic forms of the electromagnetic momentum in an *ad hoc* quantization scheme for a dispersive dielectric," Phys. Rev. A **70**, 053826 (2004).

[50] G. K. Campbell, A. E. Leanhardt, J. Mun, M. Boyd, E. W. Streed, W. Ketterle, and D. E. Pritchard, "Photon recoil momentum in dispersive media," Phys. Rev. Lett. **94**, 170403 (2005).

[51] K. J. Webb, "Dependence of the radiation pressure on the background refractive index," Phys. Rev. Lett. **111**, 043602 (2013).

[52] A. H. Velzen and K. J. Webb, "Electromagnetic force on structured metallic surfaces," Phys. Rev. B **92**, 115416 (2015).

[53] A. Einstein and J. Laub, "Über die im elektromagnetischen felde auf ruhende körper ausgeübten ponderomotorischen kräfte," Ann. Phys. **331**, 541–550 (1908).

[54] Shivanand and K. J. Webb, "Electromagnetic plane wave force on a slab," J. Opt. Soc. Am. B **29**, 3330–3334 (2012).

[55] K. J. Webb and Shivanand, "Negative electromagnetic plane-wave force in gain media," Phys. Rev. E **84**, 057602 (2011).

[56] K. J. Webb and Shivanand, "Electromagnetic field energy in dispersive materials," J. Opt. Soc. Am. B **27**, 1215–1220 (2010).

[57] Shivanand and K. J. Webb, "Electromagnetic plane-wave force on a slab having various constitutive parameters and embedded in a background material," J. Opt. Soc. Am. B **29**, 3330–3334 (2012).

[58] M. Mansuripur, "Electromagnetic-force distribution inside matter," Phys. Rev. A **88**, 023826 (2013).

[59] J. C. Maxwell, *A Treatise on Electricity and Magnetism*, vol. 2 (Dover, New York, 1954). This is an unabridged, slightly altered, republication of the third edition, published by the Clarendon Press, Oxford, in 1891.

[60] COMSOL, "Comsol multiphysics modeling software," `http://www.comsol.com`.

[61] P. B. Johnson and R. W. Christy, "Optical constants of the noble metals," Phys. Rev. B **6**, 4370–4379 (1972).

[62] K. J. Webb and J. Li, "Waveguide cavity surface-enhanced raman scattering," Phys. Rev. B **73**, 073404 (2006).

[63] K. J. Webb, "Relationship between the Einstein-Laub electromagnetic force and the Lorentz force on free charge," Phys. Rev. B **94**, 064203 (2016).

[64] A. Ashkin, J. M. Dziedzic, J. E. Bjorkholm, and S. Chu, "Observation of a single-beam gradient force optical trap fordielectric particles," Opt. Lett. **11**, 288–290 (1986).

[65] H. A. Lorentz, *The Theory of Electrons* (Dover, 1952), 2nd ed. These are notes from lectures given at Columbia University in the spring of 1906, as collected by H. A. Lorentz in 1909 and then in revised form in 1915.

[66] M. Mansuripur, "Radiation pressure and the linear momentum of the electromagnetic field," Opt. Express **12**, 5375–5401 (2004).

[67] B. A. Kemp, J. A. Kong, and T. M. Grzegorczyk, "Reversal of wave momentum in isotropic left-handed media," Phys. Rev. A **75**, 053810 (2007).

[68] M. Mansuripur, "Resolution of the Abraham-Minkowski controversy," Opt. Comm. **283**, 1997–2005 (2010).

[69] C. Baxter and R. Loudon, "Radiation pressure and photon momentum in dielectrics," J. Mod. Opt. **57**, 830–842 (2010).

[70] S. M. Barnett, "Resolution of the Abraham-Minkowski dilemma," Phys. Rev. Lett. **104**, 070401 (2010).

[71] K. J. Webb and Shivanand, "Electromagnetic plane-wave forces on homogeneous material," J. Opt. Soc. Am. B **29**, 1904–1910 (2012).

[72] K. J. Chau and H. J. Lezec, "Revisiting the Balazs thought experiment in the case of a left-handed material: electromagnetic-pulse-induced displacement of a dispersive, dissipative negative-index slab," Opt. Express **20**, 10138–10162 (2012).

[73] M. Mansuripur, "Trouble with the Lorentz law of force: incompatibility with special relativity and momentum conservation," Phys. Rev. Lett. **108**, 193901 (2012).

[74] B. Kemp, "Resolution of the Abraham-Minkowski debate: Implications for the electromagnetic wave theory of light in matter," J. Appl. Phys. **109**, 111101 (2011).

[75] W. Shockley, "Hidden linear momentum related to the $\vec{\alpha} \cdot \vec{e}$ term for a Dirac-electron wave packet in an electric field," Phys. Rev. Lett. **20**, 343–346 (1968).

[76] I. Liberal, I. Ederra, R. Gonzalo, and R. W. Ziolkowski, "Electromagnetic force density in electrically and magnetically polarizable media," Phys. Rev. A **88**, 053808 (2013).

[77] E. H. Hall, "On the rotational coefficient in nickel and cobalt," Philos. Mag. **12**, 157 (1881).

[78] M. S. Cohen, "Lorentz microscopy of small ferromagnetic particles," J. Appl. Phys. **36**, 1602–1611 (1965).

[79] M. Cohen, "Magnetic measurements with lorentz microscopy," IEEE Trans. Magnetics **1**, 156–167 (1965).

[80] J. D. Jackson, *Classical Electrodynamics* (Wiley, New York, NY, 1999), 3rd ed.

[81] R. Karplus and J. M. Luttinger, "Hall effect in ferromagnetics," Phys. Rev. **95**, 1154–1160 (1954).

[82] N. Nagaosa, J. Sinova, S. Onada, A. H. MacDonald, and N. P. Ong, "Anomalous Hall effect," Rev. Mod. Phys. **82**, 1539–1592 (2010).

[83] F. Rasetti, "Deflection of mesons in magnetized iron," Phys. Rev. **66**, 1–5 (1944).

[84] H. W. Fuller and M. E. Hale, "Determination of magnetization distribution in thin films using electron microscopy," J. Appl. Phys. **31**, 238–248 (1960).

[85] M. Mansuripur, "The force law of classical electrodynamics: Lorentz versus einstein and laub," in "SPIE NanoScience+ Engineering," (International Society for Optics and Photonics, 2013), pp. 88100K–88100K.

[86] J. H. Van Vleck, *The Theory of Electric and Magnetic Susceptibilities* (Oxford University Press, 1932).

[87] C. Kittel, *Introduction to Solid State Physics* (Wiley, 1986).

[88] K. J. Webb and A. Ludwig, "Semiconductor quantum dot mixture as a lossless negative dielectric constant optical material," Phys. Rev. B **78**, 153303 (2008).

[89] A. Ashkin and J. M. Dziedzic, "Radiation pressure on a free liquid surface," Phys. Rev. Lett. **30**, 139–142 (1973).

[90] Y.-C. Hsueh, L.-F. Yang, and K. J. Webb, "Enhanced optical pressure with asymmetric cavities," Phys. Rev. B **99**, 045437 (2019).

[91] L.-F. Yang, A. Datta, Y.-C. Hsueh, X. Xu, and K. J. Webb, "Demonstration of enhanced optical pressure on a structured surface," Phys. Rev. Lett. **122**, 083901 (2019).

[92] O. Arcizet, T. Briant, A. Heidmann, and M. Pinard, "Beating quantum limits in an optomechanical sensor by cavity detuning," Phys. Rev. A **73**, 033819 (2006).

[93] K. J. Webb and Shivanand, "Negative electromagnetic plane-wave force in gain media," Phys. Rev. E **84**, 057602 (2011).

[94] A. Mizrahi and L. Schächter, "Electromagnetic forces on the dielectric layers of the planar optical bragg acceleration structure," Phys. Rev. E **74**, 036504 (2006).

[95] M. I. Antonoyiannakis and J. B. Pendry, "Electromagnetic forces in photonic crystals," Phys. Rev. B **60**, 2363 (1999).

[96] K. J. Webb and J. Li, "Analysis of transmission through small apertures in conducting films," Phys. Rev. B **73**, 033401 (2006).

[97] K. J. Webb and Shivanand, "Electromagnetic field energy in dispersive materials," J. Opt. Soc. Am. B **27**, 1215–1220 (2010).

[98] M. C. Sanchez, E. Martin, and J. M. Zamarro, "Unified and simplified treatment of techniques for characterising transmission, reflection or absorption resonators," **137**, 209–212 (1990).

[99] P. J. Petersan and S. M. Anlage, "Measurement of resonant frequency and quality factor of microwave resonators: Comparison of methods," J. Appl. Phys. **84**, 3392–3402 (1998).

[100] S. Kim, Y. Xuan, V. P. Drachev, L. T. Varghese, L. Fan, M. Qi, and K. J. Webb, "Nanoimprinted plasmonic nanocavity arrays," Opt. Express **21**, 15081–15089 (2013).

[101] Y.-C. Hsueh and K. J. Webb, "Electromagnetic field control with binary aperiodic nanostructures," J. Opt. Soc. Am. B **34**, 2059–2071 (2017).

[102] J. R. Moffitt, Y. R. Chemla, S. B. Smith, and C. Bustamante, "Recent advances in optical tweezers," Annu. Rev. Biochem. **77**, 205–228 (2008).

[103] Y.-C. Hsueh, L.-F. Yang, and K. J. Webb, "Optical pressure control with aperiodic nanostructured material," J. Opt. Soc. Am. B **36**, 1408–1419 (2019).

[104] T. Ul Haq, K. J. Webb, and N. C. Gallagher, "Scattering optimization method for the design of compact mode converters for waveguides," IEEE Trans. Microw. Theory Techn. **43**, 559–565 (1995).

[105] T. Ul Haq, K. J. Webb, and N. C. Gallagher, "Optimized irregular structures for spatial-and temporal-field transformation," IEEE Trans. Microw. Theory Techn. **46**, 1856–1867 (1998).

[106] M.-C. Yang, J.-H. Li, and K. J. Webb, "Functional field transformation with irregular waveguide structures," Appl. Phys. Lett. **83**, 2736–2738 (2003).

[107] M.-C. Yang, J.-H. Li, and K. J. Webb, "Functional waveguide mode transformers," IEEE Trans. Microw. Theory Techn. **52**, 161–169 (2004).

[108] M.-C. Yang, H. Chen, K. J. Webb, S. Minin, S. L. Chuang, and G. R. Cueva, "Demonstration of mode conversion in an irregular waveguide," Opt. Lett. **31**, 383–385 (2006).

[109] H.-T. Chen and K. J. Webb, "Silicon-on-insulator irregular waveguide mode converters," Opt. Lett. **31**, 2145–2147 (2006).

[110] J.-H. Li, K. J. Webb, G. J. Burke, D. A. White, and C. A. Thompson, "Design of near-field irregular diffractive optical elements by use of a multiresolution direct binary search method," Opt. Lett. **31**, 1181–1183 (2006).

[111] D. Middleton, *An Introduction to Statistical Communication Theory* (IEEE Press, 1996).

[112] B. Noble and J. W. Daniel, eds., *Applied Linear Algebra* (Prentice Hall, Englewood Cliffs, New Jersey, 1977).

[113] M. Bethune-Waddell and K. J. Chau, "Simulations of radiation pressure experiments narrow down the energy and momentum of light in matter," Rep. Prog. Phys. **78**, 122401 (2015).

[114] A. Mizrahi and Y. Fainman, "Negative radiation pressure on gain medium structures," Opt. Lett. **35**, 3405–3407 (2010).

[115] A. Novitsky, C.-W. Qiu, and H. Wang, "Single gradientless light beam drags particles as tractor beams," Phys. Rev. Lett. **107**, 203601 (2011).

[116] S. Sukhov and A. Dogariu, "Negative nonconservative forces: optical "tractor beams" for arbitrary objects," Phys. Rev. Lett. **107**, 203602 (2011).

[117] M. I. Petrov, S. V. Sukhov, A. A. Bogdanov, A. S. Shalin, and A. Dogariu, "Surface plasmon polariton assisted optical pulling force," Laser Photonics Rev. **10**, 116–122 (2016).

[118] D. E. Aspnes and A. A. Studna, "Dielectric functions and optical parameters of Si, Ge, GaP, GaAs, GaSb, InP, InAs, and InSb from 1.5 to 6.0 eV," Phys. Rev. B **27**, 985 (1983).

[119] K. Seal, D. A. Genov, A. K. Sarychev, H. Noh, V. M. Shalaev, Z. C. Ying, X. Zhang, and H. Cao, "Coexistence of localized and delocalized surface plasmon modes in percolating metal films," Phys. Rev. Lett. **97**, 206103 (2006).

[120] A. Cazé, R. Pierrat, and R. Carminati, "Spatial coherence in complex photonic and plasmonic systems," Phys. Rev. Lett. **110**, 063903 (2013).

[121] J. Rosenberg, Q. Lin, and O. Painter, "Static and dynamic wavelength routing via the gradient optical force," Nat. Photonics **3**, 478–483 (2009).

[122] D. Nikolova, S. Rumley, D. Calhoun, Q. Li, R. Hendry, P. Samadi, and K. Bergman, "Scaling silicon photonic switch fabrics for data center interconnection networks," Opt. Express **23**, 1159–1175 (2015).

[123] R. Sarma, A. G. Yamilov, S. Petrenko, Y. Bromberg, and H. Cao, "Control of energy density inside a disordered medium by coupling to open or closed channels," Phys. Rev. Lett. **117**, 086803 (2016).

[124] S. Kim, Y. Xuan, V. P. Drachev, L. Y. Varghese, L. Fan, M. Qi, and K. J. Webb, "Nanoimprinted plasmonic nanocavity arrays," Opt. Express **21**, 15081–15089 (2013).

[125] E. C. Kinzel, P. Srisungsitthisunti, Y. Li, A. Raman, and X. Xu, "Extraordinary transmission from high-gain nanoaperture antennas," Appl. Phys. Lett. **96**, 211116 (2010).

[126] E. C. Kinzel and X. Xu, "Extraordinary infrared transmission through a periodic bowtie aperture array," Opt. Lett. **35**, 992–994 (2010).

[127] S. Uppuluri, E. C. Kinzel, Y. Li, and X. Xu, "Parallel optical nanolithography using nanoscale bowtie aperture array," Opt. Express **18**, 7369–7375 (2010).

[128] N. Murphy-DuBay, L. Wang, E. C. Kinzel, S. Uppuluri, and X. Xu, "Nanopatterning using nsom probes integrated with high transmission nanoscale bowtie aperture," Opt. Express **16**, 2584–2589 (2008).

[129] L. Wang, S. M. Uppuluri, E. X. Jin, and X. Xu, "Nanolithography using high transmission nanoscale bowtie apertures," Nano Lett. **6**, 361–364 (2006).

[130] J. Canny, "A computational approach to edge detection," in "Readings in Computer Vision," (Elsevier, 1987), pp. 184–203.

[131] S. Gigan, H. R. Böhm, M. Paternostro, F. Blaser, G. Langer, J. B. Hertzberg, K. C. Schwab, D. Bäuerle, M. Aspelmeyer, and A. Zeilinger, "Self-cooling of a micromirror by radiation pressure," Nature **444**, 67 (2006).

[132] A. Schliesser, P. Del'Haye, N. Nooshi, K. J. Vahala, and T. J. Kippenberg, "Radiation pressure cooling of a micromechanical oscillator using dynamical backaction," Phys. Rev. Lett. **97**, 243905 (2006).

[133] A. Dorsel, J. D. McCullen, P. Meystre, E. Vignes, and H. Walther, "Optical bistability and mirror confinement induced by radiation pressure," Phys. Rev. Lett. **51**, 1550 (1983).

[134] T. J. Kippenberg, H. Rokhsari, T. Carmon, A. Scherer, and K. J. Vahala, "Analysis of radiation-pressure induced mechanical oscillation of an optical microcavity," Phys. Rev. Lett. **95**, 033901 (2005).

[135] H. Zhu, F. Yi, and E. Cubukcu, "Plasmonic metamaterial absorber for broadband manipulation of mechanical resonances," Nat. Photonics **10**, 709 (2016).

[136] L.-F. Yang and K. J. Webb, "Pushing and pulling optical pressure control with plasmonic surface waves," Phys. Rev. B **103**, 245124 (2021).

[137] H. A. Atwater, A. R. Davoyan, O. Ilic, D. Jariwala, M. C. Sherrott, C. M. Went, W. S. Whitney, and J. Wong, "Materials challenges for the starshot lightsail," Nature materials **17**, 861 (2018).

[138] K. J. Webb and J. Li, "Resonant slot optical guiding in metallic nanoparticle chains," Phys. Rev. B **72**, 201402R (2005).

[139] K. J. Webb and J. Li, "Resonant waveguide field enhancement in dimers," Opt. Lett. **31**, 3348 (2006).

[140] K. J. Webb and J. Li, "Analysis of transmission through small apertures in conducting films," Phys. Rev. B **73**, 33401 (2006).

[141] J. Li and K. J. Webb, "Terahertz field enhancement in doped semiconductor slot cavities," J. Appl. Phys. **106**, 124901 (2009).

[142] S. A. Maier, *Plasmonics: Fundamentals and Applications* (Springer Science & Business Media, 2007).